Microplasmas: A Review

A.P. Papadakis[*,1], S. Rossides[2] and A.C. Metaxas[3]

[1]*Department of Electrical Engineering, Frederick University, Pallouriotissa, 1036, Nicosia, Cyprus*

[2]*Department of Mechanical Engineering, Frederick University, Pallouriotissa, 1036, Nicosia, Cyprus*

[3]*St John's College, University of Cambridge, CB2 1TP, Cambridge, UK*

Abstract: In this paper, a review on microplasma discharges is conducted. The different types and configurations used in microplasmas such as the Cathode Boundary Layer (CBL), Dielectric Barrier Discharge (DBD), Capillary Plasma Electrode Discharge (CPED), Inverted Square Pyramid (ISP), Square Cross Sectional Cavities (SCSC), Radio Frequency Inductively Coupled Discharge (RFIC), Radio Frequency Capacitive Coupled Discharge (RFCC), Micro-Hollow Cathode Discharge (MHCD), and microstrip technology (MS) discharges at different operating conditions are discussed. Numerical and experimental methods used for the analysis of the physics involved in these microplasmas, as well as the different construction methods used, are also described.

Keywords: Microplasmas, numerical modeling, experimental modeling, microplasma applications, review.

INTRODUCTION

Gas discharge plasmas are utilized in a variety of applications such as light sources, plasma display panels, lasers, etching of surfaces and deposition of thin layers in the semiconductor industry. In addition, uses are found in surface modification, deposition of protective coating, in analytical chemistry (for the analysis of mainly solid materials), biotechnological and environmental applications [1].

Gas discharge characteristics are generally dependent on the pressure-distance product (Pd). In order to produce stable glow discharges, one needs to lie within a certain range of Pd product. According to Foest *et al.,* [2], stable glow discharge plasmas at elevated pressures can be generated and maintained easily when the plasma is spatially confined to cavities with dimensions below 1 mm, the so-called microplasmas. Consequently, over the last few years, there has been an increased interest in the field of microplasmas driven by their ability to produce stable glow discharges, thereby triggering an increasing number of potential applications. This interest has resulted in numerous reviewed and research papers [2-7], conference workshops [8-14], symposiums [15-17] as well as a cluster issue on microplasmas [18].

Generally, microplasmas have the prospect of being used in various medical and industrial applications including: sterilization, medical treatment of human skin, surface activation, nanomaterial synthesis, and thin film coating [19]. To date, microplasmas have been developed for local medical treatment of skin diseases, and especially for the treatment of corneal infections [20]. Furthermore, the ability of the medical microplasma system to sterilize a surface has been demonstrated by Misyn *et al.,* [21]. Microplasmas are used for the remediation of volatile organic compounds (VOCs) and in biological decontamination. A growing number of laboratories are investigating microplasma generation as an excitation source for portable sensors and chemical analysis. This work has been summarized by Karanassios [5] and includes examples of atomic emission and mass spectrometry using microplasma excitation sources. Sankaran *et al.,* [22] has also reported the usage of microplasma to create silicon nanoparticles through short residence-time growth. These particles were 1-3 nm in size and also exhibited charging from the microplasma.

In the work of Mariotti *et al.,* [6], microplasmas are discussed in applications related to the synthesis of nanomaterials. Some of the applications include the injection of vapour-phase precursors into a microplasma, nucleating nanoparticles homogenously. Additionally, by evaporating solid electrodes, a number of metal or metal-oxide nanostructures of various compositions and morphologies are constructed. Finally, microplasmas were found to reduce aqueous metal salts and to produce colloidal dispersions of nanoparticles when mixed with liquids.

A review on plasma medicine is presented by Kong *et al.,* [7], focusing on plasma interaction with prokaryotic cells (bacteria), DNA, eukaryotic cells (mammalian cells) and cell membranes. The delivery of medically active 'substances' at the molecular or ionic level through effects on cell walls (permeabilization), cell excitation (paracrine action) and the introduction of reactive species into cell cytoplasm are thoroughly discussed. Additionally the effects of the electric fields, charging of surfaces and current flow in room temperature atmospheric pressure microplasmas are also analyzed.

According to Fridman *et al.,* [23] an increased interest in the use of microplasmas for bio-medical applications has developed recently. The microplasmas are able to generate

*Address correspondence to this author at the Department of Electrical Engineering, Frederick University, Pallouriotissa, 1036, Nicosia, Cyprus; Tel: 0035799334791; Fax: 0035722108532;
E-mails: eng.ap@frederick.ac.cy, papadaki@ucy.ac.cy, ap263@cam.ac.uk

1874-1835/11

diffuse atmospheric pressure plasmas with dimensions between 10-500 μm that can be used in medical diagnostics and environmental sensing. Becker and his colleagues [3, 24] have been able to develop different microplasma sources which can be used for the removal of VOCs, suitable for remediation of gaseous waste streams, detection of trace contaminants in gas flow, generation of high intensity ultraviolet (UV) radiation, and sources suitable for micro-sized plasma reactors. Regarding the temperatures observed in these microplasmas, the temperatures can vary from room temperature in noble gases to 2000 °K in molecular gases.

Ozone generation efficiency is traditionally produced using Dielectric Barrier Discharges (DBD). It is now suggested [25] that the efficiencies for ozone production can be improved by utilizing atmospheric pressure Micro-Hollow Cathode Discharge (MHCD) and Capillary Plasma Electrode Discharge (CPED).

Generally, in microplasmas one should bear in mind that the interface between the plasma and the solid boundary considerably affects the discharge characteristics, due to the large ratio of surface area to the plasma volume, which makes the characterization of plasma-surface interactions necessary. Since microplasmas are in a non-equilibrium state, they have applications related to functional material synthesis, micro-electromechanical systems, ultra-short wavelength light sources, and active plasma devices [26].

In order to analyze the physics involved in the above microplasma devices, one can either use experimental and/or numerical techniques. To study the microplasma behaviour experimentally, various techniques are discussed as well as methods used for the micromachining of the microplasma devices.

For the numerical characterisation of microplasmas, kinetic and fluid analysis models are discussed. Special emphasis in this paper is attributed to fluid models which are capable of analyzing these microplasma discharges efficiently, provided that the charges exhibit Maxwellian velocity distributions. To analyze the charged plasma behaviour of electron, positive and negative ions' in microplasmas one needs to solve the conservation for charges equations coupled to Poisson's equation to account for the electric field, and the Navier-Stokes equations to account for the neutral gas dynamics such as gas heating effects. Consequently, for the numerical analysis and characterization of microplasmas, the formulation of the necessary equations able to capture the physics is identified and a specific numerical method to solve the above equations is discussed. In the equations, all the important physics phenomena such as total conductive, displacement and external currents, photoemission and photoionization effects are described. Furthermore, the various methods for calculating the transport properties of the different gases used in microplasma fluid modelling are also identified and discussed.

In brief, this paper discusses the different configurations used to generate microplasmas. It also reviews recent advances in the field of microplasmas, and points to future trends and their prospective applications. The aim of this paper is to provide all the necessary tools and information for researchers who are new to the field, to conduct research in the emerging field of microplasmas.

MICROPLASMA CONFIGURATIONS

According to Ishii [26] and Yokoyama *et al.,* [27], different types of microplasmas are classified into roughly three modes, namely, concentrated energy mode, space-limited mode and mass-limited mode. In the concentrated energy mode, the microplasma is generated at the electrode tips with concentrated high electric field strengths [28] and therefore high electrical energy. In the space-limited mode, the microplasma volume is limited by solid boundaries such as microcells or capillaries found in plasma display panels. In the mass-limited mode, the microdischarge develops between electrodes using an initial material such as powder, or droplet with no surrounding walls.

There are many different types of microplasma configurations which are discussed below:

Cathode Boundary Layer Microplasma (CBL)

Fig. (**1**) shows the typical configuration of a CBL discharge [29-31]. It is a DC glow discharge and consists of a planar cathode and a ring-shaped anode. In this configuration, the discharge is restricted to the cathode fall and the negative glow which serve as a virtual anode. The CBL is found to be an efficient source of excimer radiation. It exhibits a positive slope for the current-voltage characteristics over a wide range of currents, which permits the parallel operation of such devices without the need for any ballast resistors. Belinov [30] shows that there is no need to deploy special techniques to explain patterns of glow cathodes [32, 33], but rather traditional glow discharge analysis using drift/diffusion approximation for the charged carriers, including volume ionization, attachment, recombination, and secondary electron emission.

The lifetime operation of DC microdischarges is of the order of a few hours since the surface of the microplasma is destroyed from the sputtering effect, forcing the microplasma to cease to exist [34, 35]. Regarding the scales of the CBL discharge, the diameter of the cylindrical cavity is in the range of a fraction to several millimetres, and the dielectric has a typical thickness of the order of 100 μm and with a cavity of the same diameter as the anode [3].

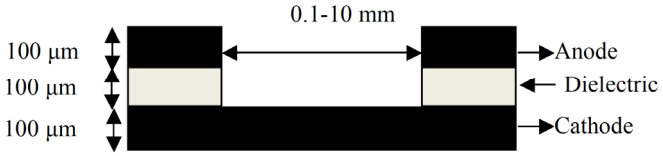

Fig. (1). Typical configuration of a CBL microplasma.

Dielectric Barrier Discharge Microplasma (DBD)

A DBD microplasma is a discharge which uses dielectric boundaries to prevent the discharge to transit into an arc by prohibiting the charges being absorbed into the electrodes. A typical DBD microplasma configuration is shown in Fig. (**2**) that consists of a planar dielectric barrier discharge with two electrodes coated with an insulating layer, forming an air gap between them for the microplasma discharge to develop at low power operation of less than 250 mW. An atmospheric pressure air microplasma ionization source has been

successfully constructed with operational lifetimes in excess of 5000 hours [36]. The frequencies of operation are as low as several kHz to greater than 20 MHz. Using the technique described in [37], the neutral gas temperature calculated using the rotational temperature of the second positive system of N_2 was found to remain at ambient, suggesting preferable ionization conditions for chemical analysis applications. An extensive review of the different DBD configurations utilized for microplasma applications can be found in [38].

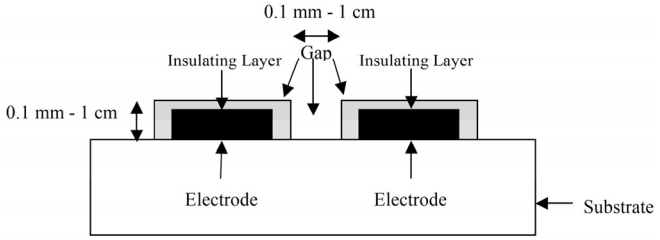

Fig. (2). Typical configuration of a DBD.

Capillary Plasma Electrode Discharge Microplasma (CPED)

The CPED as shown schematically in Fig. (**3**) is a variant of the barrier configuration invented by Kunhardt *et al.,* [39], which obtained plasmas with electron densities above 10^{12} cm^{-3}. In the CPED, dielectric capillaries are used that cover one or both electrodes of a discharge device, and as a consequence, the CPED discharge exhibits a mode of operation that is not observed in DBDs, the so-called "capillary jet mode" [40]. The idea behind the dielectric capillaries is to suppress the glow-to-arc transition instability by stabilizing the cathode fall region of the discharge. It can be driven both by DC and AC voltages, depending on the application. The CPED reactors have applications in the display, semiconductor, storage disk and optical communications industries, with implications in the etching/cleaning of electronic structures, surface modification, medical sterilization and thin film deposition processes. For example, cleaning of metal surfaces such as Al (or stainless steel) has been achieved using novel CPED plasma operating in atmospheric-pressure ambient air, and by monitoring the power, plasma density, residence time and feed gas composition. The hydrocarbon removal rates were almost 100% for residence times of only a few seconds [41].

Panikov *et al.,* [42] have utilized CPED plasma reactors for the destruction of spore-forming bacteria, which are believed to be among the most resistant micro-organisms. Optical emission spectroscopy (OES) and other plasma diagnostic studies have shown that these discharges when compared to other atmospheric-pressure discharge plasmas experience lower sustained voltage of the order of a few hundred volts, lower energy input density and higher average electron energy at lower gas temperatures.

A diffuse mode of operation is observed at low frequencies of the order of a few kHz and plasma bright jets are observed above a certain threshold frequency. The threshold frequency depends on the length and diameter of the capillary holes used. As the distance between the capillary holes decreases, the discharge exhibits a uniform phase since they overlap. The capillary holes due to their non-uniform geometry enhance ionization phenomena and at the same time allow direct contact with the metal electrode. The non-uniform shape of the capillaries enhances the electric field, which in turn enhances ionization by providing much more energetic electrons than in a uniform geometrical electrode. Due to the existence of capillaries on one of the electrodes, the current pulses observed are shown to be asymmetric. Studies of the He discharge for similar configurations have shown that for the diffuse mode, electron densities observed were of the order of 10^{10} cm^{-3}, whereas for the capillary mode were of the order of 10^{12} cm^{-3}. However, in another study by Panikov *et al.,* [42], electron densities of up to 10^{14} cm^{-3} were observed.

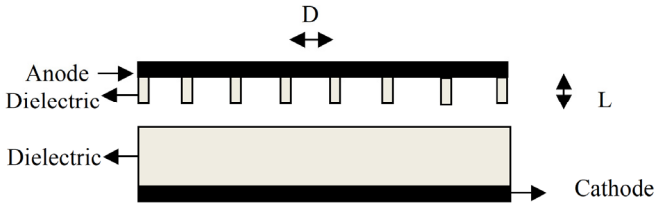

Fig. (3). Capillary plasma electrode discharge (CPED) configuration.

The capillaries have typical diameters in the range of D = 0.01-1 mm and length-to-diameter ratios (L/D) of the order of 10:1 or 1:1 [3, 43] and their operation is limited to hundreds of microseconds.

Micro-Hollow Cathode Discharge Microplasma (MHCD)

A MHCD consists of two closely spaced hollow electrodes separated by a dielectric layer with a voltage applied between them. Fig. (**4**) shows a typical configuration of a MHCD. The diameter of the hole and the thickness of the dielectric are of the order of some hundreds of microns.

According to Shi *et al.,* [44], the MHCD exhibits three distinct regions of operation, the Townsend mode at low current, the hollow discharge mode and the abnormal glow mode. Within the Townsend and the abnormal modes, the discharge operates at positive current-voltage characteristics and therefore it can be used in parallel operation of microdischarge devices without the use of any ballast resistors. Shi *et al.,* have managed parallel operation of MHCD in DC argon discharges without the use of ballast resistors by extending the operating regime of positive current-voltage characteristic of the discharge.

Meyer *et al.,* [45] have shown that the lifetime operation of a MHCD when compared to that of a DC microplasma discharge reduces the electrode sputtering by a factor of 6.5, therefore extending the lifetime operation of these microplasmas into a similar range. Long term operation of DC and MHCD are of the order of a few hours, for example 17 hours in a particular case. The size of the diameter of a typical MHCD is of the order of 250 μm [43].

Stable direct current glow discharges at atmospheric pressure air using MHCD as plasma cathode were also generated by Abdel-Aleam *et al.,* [46] with lengths from 1 mm to 2 cm and attaining electron densities between 10^{11}-10^{13} cm^{-3}. The sustaining voltage was increased linearly with the length of the microplasma, and at currents of 10 mA, the electron densities exceeded 10^{13} cm^{-3} close to the cathode, and reduced to 10^{11} cm^{-3} as one moved away from the cathode. In the case of two microdischarges operating in

parallel at a current of 8.5 mA, the two discharge plasmas were found to merge for gaps larger than 0.5 cm, when their axes were separated by a distance of 0.4 cm.

Schoenbach and co-workers [47] have been able to produce stable atmospheric-pressure microplasmas up to power densities of 100 $kWcm^{-3}$. These MHCDs can be utilized as plasma cathodes for generating a diffuse discharge between the MHCD cathode and a third positively-biased electrode placed some distance away. This is the so-called Micro-Cathode Sustained Discharge (MCSD) configuration, which can be operated as a non self-sustained discharge.

MCSD constructed by Schoenbach and co-workers [47] operate at DC and exhibit positive voltage-current characteristics and allow parallel operation without the need for any ballast resistors. Alexeff *et al.,* [48] have also demonstrated the operation of a large-area DC discharge at atmospheric-pressure, making use of a water-impregnated, high-resistivity cathode.

According to Puech [49], the MCSD appears as a unique tool for producing at high pressure, large fluxes of $O^2(\alpha^1\Delta_g)$ metastable states. Schoenbach [50] suggests that, in order to achieve stable operation of MHCD one needs to fine-tune the Pd product to be in the range of 0.1-10 Torr cm depending on the type of the gas, the type of the electrodes and the geometry used. MHCD generally operate under DC and pulsed conditions and exhibit cathode fall and negative glow regions in the abnormal glow regime at high pressures, with gas temperatures of the order of 2000 ^oK in air and 400 ^oK in Neon, and can be used as intense excimer emitters.

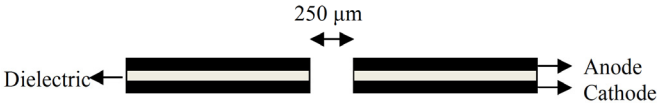

Fig. (4). Typical configuration diagram of a MHCD.

Inverted Square Pyramidal Microplasma (ISP)

Spatially uniform glow discharges at ambient atmospheric air, extending over lengths of at least 0.5-1 mm, have been produced in Si (50 μm)^2 inverted pyramidal microdischarge device. The above device serves as a plasma cathode device with a metal or dielectric anode electrode, driven at frequencies from 5-20 kHz [51, 52]. This device seems ideally suited for environmental analysis of air samples by emission spectroscopy.

The emitting aperture (pyramid base dimensions) for the device shown in Fig. (**5**) is 50 × 50 μm^2 and the thickness is of the order of 100 μm, whereas ISP microplasmas as small as 10 x 10 μm^2 have been constructed [53]. In the work of Park *et al.,* [54], more than 70% of an inverted squared pyramid array of 200 x 200 exhibited the initial radiative power after 100 hours of continuous operation.

Square Cross-Sectional Cavities Microplasma (SCSC)

SCSC microplasmas have been shown by Park *et al.,* [55] to be used as UV radiation sources by utilizing the formation of XeO excimer microplasmas [3]. SCSC microplasmas constructed by El-Habachi and Schoenbach [56] reached efficiencies of 8% for Xe excimer microplasma sources. Arrays of microplasma devices fabricated using square/circular cross-sectional microcavities in a photodefinable glass were also constructed by Kim *et al.,* [57], in which each pixel has a circular or rectangular cross section and a characteristic dimension of 75-100 μm. The microplasmas have the ability to be driven either by DC or AC applied voltage. Arrays as large as 25 x 25 pixels have been tested operating in the abnormal glow regime in Ne pressures between 200-700 Torr [58]. A typical configuration of an SCSC microplasma discharge developed by Kim *et al.,* [58] is shown in Fig. (**6**).

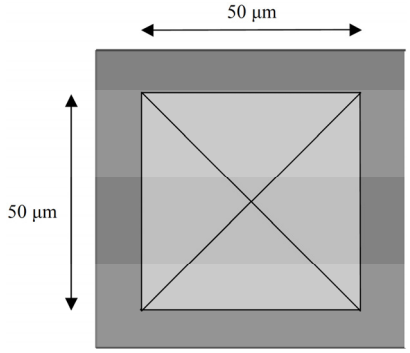

Fig. (5). Typical configuration of an ISP microplasma.

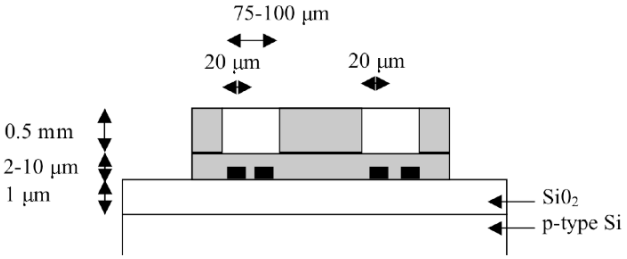

Fig. (6). Typical configuration of an SCSC microplasma discharge developed by Kim *et al.,* [57].

Radio Frequency Inductively Coupled Microplasma (RFIC)

RFIC microplasmas are electrode-less discharges which utilize induction through a coil wrapped around a dielectric wall to generate microplasmas as shown in Fig. (**7**). The electric fields generated are usually parallel to the dielectric walls, thereby minimizing the sputtering effect which, in general, prohibits the prolonged operation of microplasmas. However, an RFIC, when operated at high pressures in order to obtain large densities of charged species, becomes inefficient due to the increased surface to volume ratio, as well as due to the fact that the inductance of the coil decreases faster than the parasitic resistance. A solution is to operate them at higher frequencies such as in the VHF and UHF bands; however, the maximum frequency of operation is limited by the AC resistance and the self-resonance frequency of the coil, as well as from the electron collision frequency [34].

Radio Frequency Capacitive Coupled Microplasma (RFCC)

RFCC at high pressures tend to be constricted and easily transit to arcs, therefore dielectric layers are often used to prevent charges from entering the electrodes, thus prohibiting the development of the sheath near the electrodes, and thereby the transition to an arc [34]. Fig. (**8**).

shows a typical configuration of a RFCC microplasma discharge which has an inter-electrode gap of 65-500 μm.

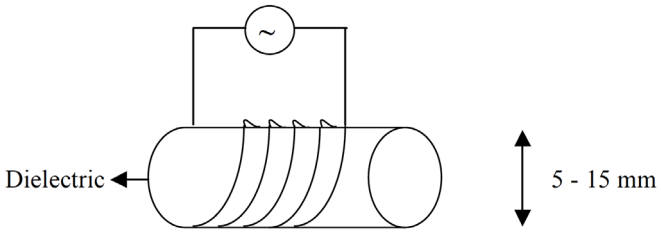

Fig. (7). Typical configuration of a RFIC microplasma discharge.

In contrast with the RFIC, the electric field is perpendicular to the dielectric walls, with the consequent effect that sputtering prohibits their lifetime operation, as well as the pressures of operation. Studies have shown that when operating these discharges above the Radio Frequency (RF) region, a reduction in the breakdown voltage occurs [59] and the efficiency increases [60].

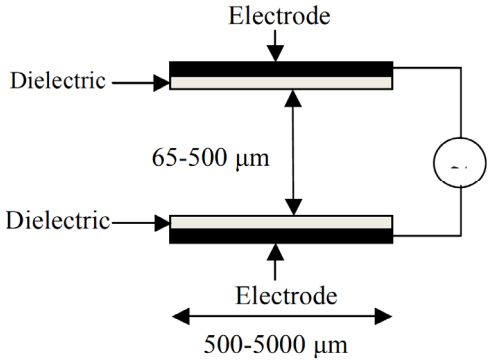

Fig. (8). Typical configuration of a RFCC microplasma discharge.

Microstrip Microplasma (MS)

MS microplasmas utilize microstrip technology to transfer electromagnetic fields into a small air gap in order to generate microplasma. A typical schematic diagram of a split-ring resonator microplasma source is shown in Fig. (**9**).

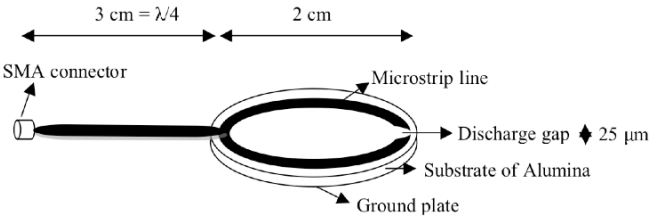

Fig. (9). Typical configuration of a MS split-ring resonator.

Hopwood *et al.,* [61] have utilized microstrip transmission line technology in the form of a split-ring resonator to ignite and sustain 25 μm wide discharge microplasma between two co-planar gold electrodes. The golden electrodes were the two ends of a microstrip transmission line that was microfabricated on an Al_2O_3 substrate at a resonant frequency of 895 MHz. Within the microplasma, optical emission in the UV region was obtained, and no plasma induced erosion was observed after 50 hours of continuous operation.

For the detection, as well as size distribution of nanoparticles, it is necessary to electrically charge the particles and then classify them depending on their individual mobilities. This particle classification is commonly performed using a Differential Mobility Analyzer (DMA) [62]. In their work, Xue and Hopwood [63] have generated argon microplasmas in a 350 μm microstrip transmission line discharge. This microplasma device is alternatively used for the classification and detection of nanoparticles by basically negatively charging the microparticles using stray electrons, directing them towards the potential well of the microplasma, and therefore trapping the nanoparticles within the microplasma. The balancing of the electrostatic force of the potential well against the molecular drag force enables the trapping of the particles. The nanoparticles retain the negative charge after the microplasma is extinguished, which can later be electrostatically detected and identified.

Hopwood *et al.,* [61] microstrip technology has been shown to offer a major advantage in atmospheric-pressure air microplasmas in comparison to the other methods, as it minimizes the ion sputtering effect on the dielectric walls without the use of any flow gases, As such, their lifetime operation is extended, as well as improving the power consumption, cost and ease of manufacture of these microdevices.

In a latest work by Hopwood and co-workers [64], a microstrip split-ring resonator (MSRR) discharge operating at 1.8 GHz in atmospheric-pressure helium was constructed capable of being used as an excitation source. Microwave power of 0.2 W is necessary to continuously maintain the microplasma with no electrode damage. It was used for chemical detection and as a sensor for gas chromatography.

Jaeho *et al.,* [65] have used an alternative to the split-ring resonator microstrip technology in order to generate atmospheric-pressure air microplasmas. Fig. (**10**) shows such a configuration which comprises of a microwave source, a stub element for matching purposes, an electrode aluminium strip, alumina protrusions and an etched air gap for the microplasma to develop. In a recent work by Gregorio *et al.,* [66], microplasmas within gaps of 50-200 μm were created using the microstrip transmission line technology.

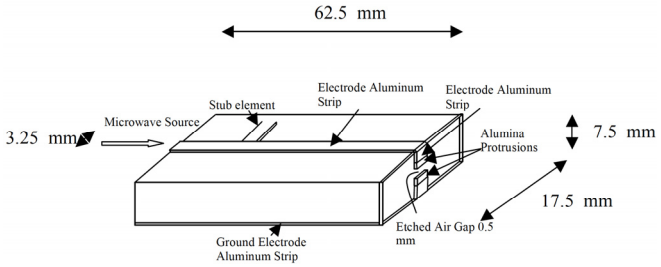

Fig. (10). Typical microstrip configuration using a microwave source [65].

The plasma temperatures were measured using OES, whereas the electron densities using Stark broadening measurements of the H_β line-emission profile. The rotational and vibrational temperatures in air were between the ranges 950-1400 ^oK and 5200-5800 ^oK respectively, whereas in argon the rotational and excitational temperatures were 550-630 ^oK and 5800 ^oK, respectively. High electron densities of the order of 10^{14} cm^{-3} were observed within volumes of 10^{-4} - 10^{-3} cm^3.

Jaeho *et al.,* [65] and Gregorio *et al.,* [66] suggest using higher frequency microwave sources, of the order of 24.5 GHz, in order to allow the formation of air microplasmas at smaller sizes.

NUMERICAL ANALYSIS

To perform numerical analysis of a physical system, three important steps are necessary. Firstly, the physical problem must be clearly defined and this is achieved by identifying the characteristic quantities that best describe the physical system. The second step is to define the governing equations which relate to the characteristic quantities involved in the system. Finally, the third step is to select the appropriate numerical method to solve the selected system of equations, as well as the suitable initial and boundary conditions. Thereafter the numerical method is formulated and implemented in computer software and executed to obtain the behavior of the physical system.

To describe the state of microplasmas rigorously, it would be necessary to numerically analyze all the particle locations and velocities and describe the electromagnetic field in the plasma region. However, it is generally impossible, with the current computer resources, to keep track of all the particles in the plasma due to excess memory and processing CPU time required. Therefore, plasma physicists commonly use two different descriptions, which are less detailed, known as fluid and kinetic models.

Fluid Models

Fluid models describe partial differential equations in terms of smoothed variables such as mass, momentum and energy conservation. A frequent simplified fluid model used is the magnetohydrodynamic model, which treats the plasma as a single fluid model coupled to Maxwell and probably Navier-Stokes equations. Moving into a more detailed plasma simulation one uses the two-fluid model, where electrons and ions partial differential equations are solved separately. In order for a fluid model to be accurate, the medium generally, and in this case the plasma, must undergo a significant number of collisions such that the plasma velocity distribution function is close to that of Maxwell-Boltzmann.

Another popular fluid model utilized for plasma simulations is based on the velocity moments of the Boltzmann transport equation (continuity equations of particle density), usually coupled to Poisson's equation to calculate a self-consistent electric field distribution [67]. The drawback of this model, is that it assumes that the plasma species are more or less in equilibrium with the electric field, which is not always the case, such as in regions of high electric fields as in the cathode fall region of a high pressure glow discharge. However, by solving the Boltzmann momentum and energy transport equations, the non-equilibrium behavior of the plasma species can be accounted for.

Fluid models depend on input transport and the rate coefficients parameters and are calculated either experimentally as functions of the ratio of electric field over neutral gas density per unit volume (E/N), or numerically by solving the electron distribution Boltzmann equation. In the numerical case, the electron distribution function is generally non-Maxwellian and is calculated by utilizing the collisional cross sectional data by solving the Boltzmann equation. Commercial software packages such as ELENDIF [68], BOLSIG [69], and BOLSIG+ [70] are used to calculate the above transport parameters. Specifically, according to Hagelaar and Pitchford [71], a two-term approximation method by expanding the electron distribution in terms of Legendre polynomials of $\cos\theta$ is used to formulate a set of equations for the expansion coefficients, whereas for high E/N, as in the case of the cathode fall region of normal and abnormal glow discharges, a six-term approximation is necessary to ensure that the results are accurate [72, 73]. The presence of dielectrics in microplasmas ensures that the electric field near the electrodes will not reach extremely high values rendering the two-term approximation valid in diffused discharges, which makes the use of fluid approximations in these microplasmas ideal. Therefore depending on the type of microplasma and the fields generated, a two-term approximation can be sufficient. However there is a limit at which one can use this approximation, and not revert to higher order terms for the approximation to be sufficiently accurate, especially within cathode fall regions that have high electric fields.

In fluid simulations, physical systems are characterized by solving partial differential equations which incorporate the physical processes of the problem under investigation. These partial differential equations are classified into three major categories: elliptic, parabolic and hyperbolic. There are three different methods that are widely used for the solution of these equations, which are the Finite Difference (FD), the Finite Element (FE) and the Finite Volume (FV) methods.

An extension to these methods is the incorporation of adaptive mesh techniques to analyze fluid simulations. Adaptive mesh methods utilize error indicators to calculate gradients of the variables being analyzed and move the mesh accordingly [74]. Fine mesh resolution is used at locations of high gradients and low resolution at locations where small gradients are observed.

The FD method uses a local Taylor series expansion to approximate partial differential equations. A major disadvantage of the FD method is the usage of only regular meshes for the discretization of the partial differential equations. Therefore, in highly irregular complex geometries, finite differences are unable to capture efficiently the correct physics and FE and FV methods are preferred due to their ability to perform well in irregular geometries.

The most popular FE method used is the Galerkin FE method which is based on a set of weight functions $w(x)$ set to be the same as the basis function $N_i(x)$, with the distribution functions varying from 0 to 1. Thereafter Dirichlet boundary condition are applied, if necessary, by imposing constant values to the independent variables and forcing the weighting functions to be equal to zero at the boundaries. The Neumann boundary condition is imposed by the variational formulation automatically, which is the reason to call this boundary condition a natural boundary condition. Otherwise, one has to change the right hand side of the equation, so that it includes a boundary integral term in the variational formulation.

In the FV method [75, 76], partial differential equations are evaluated as algebraic equations. Similar to the finite difference and finite element methods, they are calculated at discrete places on a meshed geometry, with the finite volume being the small volume surrounding each node point on a mesh. Breaking space into such cells is called the Voronoi Diagram of a set of points. The FV integrals which contain a divergence term are transformed into surface integrals by using the divergence theorem and the terms are evaluated as fluxes at the surfaces of each finite volume. Since the flux entering and leaving a certain volume is identical, these methods are conservative. The advantage of the FV method over the FD method is that it easily enables the usage of unstructured meshes.

Generally, a numerical scheme is analyzed according to three different concepts which are consistency, stability and convergence [77]. Consistency of a numerical scheme is whether its discrete operator converges towards the continuous operator (with derivatives) of the partial differential equation, as the time step and mesh resolution tend to zero, thereby vanishing the truncation error. Regarding stability, one needs to consider the Courant-Friedrichs-Lewy (CFL) condition, which is the condition for the stability of explicit schemes devised by Courant, Friedrichs and Lewy in 1928. A scheme is said to be convergent if the difference between the computed solution and the exact solution of the partial differential equation decreases, as the mesh size and time stepping is decreased to zero.

There are two different methods available to solve a linear system of the form Ax=b where A is a matrix, x and b are column vectors, namely the direct and iterative methods [78]. Iterative methods use a number of steps in order to converge towards the final answer and perform well in sparse matrix and parallelized solutions, whereas direct methods such as Gaussian elimination are more accurate, albeit more computationally expensive.

The important parameters for the simulation of air microplasmas are the electric field, the electric charges as well as the neutral gas effects. Generally, the stability of the glow discharge depends on the extent of the heating of the gas since if high temperatures are reached, the air microplasma will revert into a spark or an arc and will cease to exist. Therefore if one is to generate stable glow discharges in air microplasmas, it is important that the temperature effects are taken into account as well during the air microplasma simulation. Consequently, the behavior of charged particles is calculated through the calculation of the electric field and of the behavior of the charged particles, and this is achieved by solving the Poisson equation together with the continuity equations. Regarding the behavior of neutral gas particles, the Navier-Stokes equations need to be solved to account for the neutral gas heating effects and density variations within the air microplasma. Therefore, to analyze and optimize air microplasmas, the Poison, continuity and Navier-Stokes equations are solved and coupled together. The authors have a particular interest in the simulation of ambient air microplasmas since no vacuum tubes are necessary and it is much cheaper to develop such applications. To analyze ambient air microplasmas, one must also be able to capture the important secondary physical processes which occur in microplasmas such as photoionization and photoemission.

Poisson, Continuity and Navier-Stokes Model

The characterization of microplasma phenomena requires the simultaneous solution of the Poisson equation to account for the electric field, of the charged particle continuity equations to account for the space charge and of the Navier-Stokes equations for the neutral gas changes. Papadakis *et al.,* [79], coupled this set of equations and analyzed heating effects in atmospheric discharges starting from a single electron as the initial condition. The complete fluid model is depicted below:

$$\frac{\partial N_e}{\partial t} + \nabla.(N_e \mathbf{W_e}) = S_e \quad (1)$$

$$\frac{\partial N_p}{\partial t} + \nabla.(N_p \mathbf{W_p}) = S_p \quad (2)$$

$$\frac{\partial N_n}{\partial t} + \nabla.(N_n \mathbf{W_n}) = S_n \quad (3)$$

$$-\nabla.(\varepsilon_g(\nabla V)) = q \quad (4)$$

$$\frac{\partial \rho}{\partial t} + \nabla.(\rho \mathbf{v}) = S \quad (5)$$

$$\frac{\partial(\rho \mathbf{v})}{\partial t} + \nabla.(\rho \mathbf{v}\mathbf{v}) = -\nabla P - \nabla.\boldsymbol{\tau} + \sum_s \mathbf{MT_s} \quad (6)$$

$$\frac{\partial \varepsilon}{\partial t} + \nabla.(\varepsilon \mathbf{v}) = -\nabla.(\mathbf{Q}) - \nabla.(\mathbf{v}(P\mathbf{I} + \boldsymbol{\tau})) + \sum_s \mathbf{MT_s}.\mathbf{v} + \sum_s f_{ts}\mathbf{J_s}.\mathbf{E} \quad (7)$$

where the following equations hold:

$$S_e = \alpha N_e \mid \mathbf{W_e} \mid -\eta N_e \mid \mathbf{W_e} \mid -\beta_{ep} N_e N_p + \nabla.(D_e \nabla N_e) \quad (8)$$

$$S_p = \alpha N_e \mid \mathbf{W_e} \mid -\beta_{ep} N_e N_p - \beta_{pn} N_p N_n \quad (9)$$

$$S_n = \eta N_e \mid \mathbf{W_e} \mid -\beta_{pn} N_p N_n \quad (10)$$

$$S = m(-\alpha N_e \mid \mathbf{W_e} \mid -\eta N_e \mid \mathbf{W_e} \mid +2\beta_{pn} N_p N_n + \beta_{ep} N_e N_p) \quad (11)$$

$$\mathbf{Q} = -k\nabla T \quad (12)$$

$$\mathbf{J_s} = q_s N_s \mathbf{W_s} \quad (13)$$

$$P = NKT \quad (14)$$

$$\tau_{ii} = -\mu(2\frac{\partial v_i}{\partial x_i} - \frac{2}{3}\nabla.\mathbf{v}) \quad (15)$$

$$\tau_{ij} = -\mu(\frac{\partial v_i}{\partial x_j} + \frac{\partial v_j}{\partial x_i}) \quad (16)$$

$$\mathbf{MT_s} = N_s \frac{m}{m + m_s}\frac{q_s}{\mu_s}(\mathbf{W_s} - \mathbf{v}) \quad (17)$$

$$\mathbf{E} = -\nabla V \quad (18)$$

$$q = e(-N_e + N_p - N_n) \quad (19)$$

N_e, N_p, N_n are the electron, positive and negative ion densities, e is the electron charge, $\mathbf{W_e}$, $\mathbf{W_p}$ and $\mathbf{W_n}$ the

corresponding velocity vectors, α the ionisation, η the attachment, β_{ep} the recombination between electrons and positive ions, β_{pn} the recombination between positive and negative ions and D_e the electron diffusion coefficients. The positive and negative ion diffusion coefficients are usually omitted since they have a negligible effect. Furthermore, q is the net charge density, ε_g the general permittivity, V is the potential difference, ρ the neutral gas density, **E** the electric field, ε the neutral gas thermal energy density, **I** the unit stress tensor, **v** the neutral gas velocity vector comprising of v_x, v_y and v_z components, **J** the current density, f_{ts} the percentage of energy density of charged particle with subscript s that is transferred as thermal energy to the neutral particles due to inelastic collisions, with s taking values of e, p and n for electrons, positive and negative ions, respectively, P the pressure, K is the Boltzmann constant, T the temperature, N the number of neutral gas particles per unit volume, $\mathbf{MT_s}$ the momentum transfer of charged to the neutral particles due to elastic collisions comprising of $MT_s\{x\}$, $MT_s\{y\}$, and $MT_s\{z\}$ components, μ the viscosity coefficient, m the mass of the neutral gas particles, m_s, q_s, $\mathbf{W_s}$, μ_s, the mass, charge, velocity vector and mobility of charged particle s, and **τ** the shear stress tensor which comprises of the τ_{ii} and τ_{jj} components.

Papadakis *et al.,* [79] in order to analyze heating effects in atmospheric-pressure air plasmas, have used transport parameters such as collision coefficients and drift velocities of the charged particles measured from experimental data of Morrow and Lowke [80] as a function of E/N. The charged particle continuity equations are coupled to Poisson's equation *via* the electric field strength and to the Navier-Stokes equations *via* the E/N and their pressure. Poisson's equation is coupled to the continuity equations *via* the net charge density. As far as the Navier-Stokes equations are concerned, these are coupled to Poisson's equation *via* the electric field strength and to the charged particle continuity equations *via* production and loss processes, and *via* momentum and kinetic energy exchange between charged and neutral particles.

If one wishes to include the conservation of momentum and energy density for electrons, positive and negative ions, the differential equations should have the general form:

$$\frac{\partial(\rho_s \mathbf{W_s})}{\partial t} + \nabla.(\rho_s \mathbf{W_s} \mathbf{W_s}) = -\nabla P_s - \nabla.\boldsymbol{\tau}_s - \sum_s \mathbf{MT_s} \quad (20)$$

$$\frac{\partial \varepsilon_s}{\partial t} + \nabla.(\varepsilon_s \mathbf{W_s}) = -\nabla.(\mathbf{Q_s}) - \nabla.(\mathbf{W_s}(P_s \mathbf{I} + \boldsymbol{\tau}_s)) - \sum_s \mathbf{MT_s}.\mathbf{v} - \sum_s f_{ts} \mathbf{J_s}.\mathbf{E} \quad (21)$$

Subscript s represents the electron, positive and negative ions, and the various terms are similar to the ones used for the neutral gas particle conservation equations.

Secondary production processes such as photoemission and photoionization are important in the development of a microplasma discharge. The photoemission effect can be neglected in long gaps, whereas it must be included in the analysis of short gaps where the plasma simulation interacts with the electrodes.

Photoemission Model in Air

In order to calculate the photoemission effect on the cathode, the following formula is used:

$$N_e^s = \frac{\gamma_p \, N_{eb} \, a_b \, |W_{eb}| \, V_b Z \, e^{-\mu_a c}}{|W_{es}| 4\pi c^3} \quad (22)$$

where γ_p is the photoemission coefficient, V_b is the volume of the element, N_{eb} is the number of electrons per unit volume at volume V_b, a_b is the ionization coefficient within volume V_b, which is usually a function of E/N, $\mathbf{W_{eb}}$ is the velocity of electrons within volume V_b, $\mathbf{W_{es}}$ is the velocity of electrons within surface dA, c is the distance from volume element V_b to elemental area dA, Z is the vertical distance of volume V_b from the cathode and μ_a is the absorption coefficient. Fig. (**11**) shows a schematic diagram used to calculate the photoemission depicting the elemental area of the cathode dA to undergo the photoemission due to photoemission from volume V_b.

In order to calculate the photoemission effect, the contribution from all the volume elements at a single cathode surface needs to be calculated, thereby conducting a number of numerical operations equal to the number of cathode faces multiplied by the number of volume elements within the gap. In the case where the number of operations is extremely large, one can significantly simplify the number of calculations. This is achieved by separating the grid into equally spaced regions and by interpolating the above values into the equally spaced grid and calculating the photoemission effect on that grid and then interpolating it back to the original mesh. This will of course have the effect of compromising the accuracy of the ensuing results; however it will give a very good approximate solution of the photoemission effect with reduced calculations.

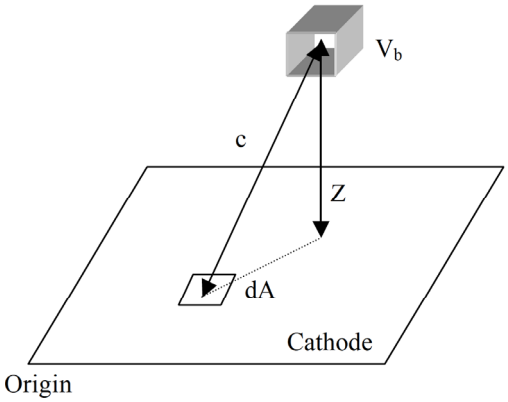

Fig. (11). Photoemission at the elemental area of the cathode dA due to photon emission from volume V_b.

To demonstrate the effect of the photoemission coefficient on the development of a microplasma discharge, we have analyzed the avalanche, streamer and glow discharge in a parallel plate configuration of 1 cm separation using three different photoemission coefficients. Therefore, Fig. (**12**) shows a one-dimensional plot of the conductive current in the microplasma versus time for three different photoemission coefficients in a parallel plate discharge gap of 1 mm at an applied DC voltage of 5600 V (20 % above the breakdown threshold voltage) in ambient atmospheric air. Three different photoemission coefficients were used,

which are most extensively quoted in the literature: 0.001 used by Morrow *et al.,* [80], 0.005 used by Kunhardt and Tzeng [81] and Steinle *et al.,* [82] and finally 0.0005 for comparison purposes with the absorption coefficient being equal to 15.2 cm^{-1}.

As far as the conductive current for three different photoemission coefficients is concened, the larger the coefficient, the more electrons are released from the cathode and therefore more ionisation collisions and avalanches that produce more current are expected. Furthermore, the higher the photoemission, the faster the formation of the avalanche the primary streamer and the glow discharge is, as shown by the time difference among the three curves in Fig. (**12**).

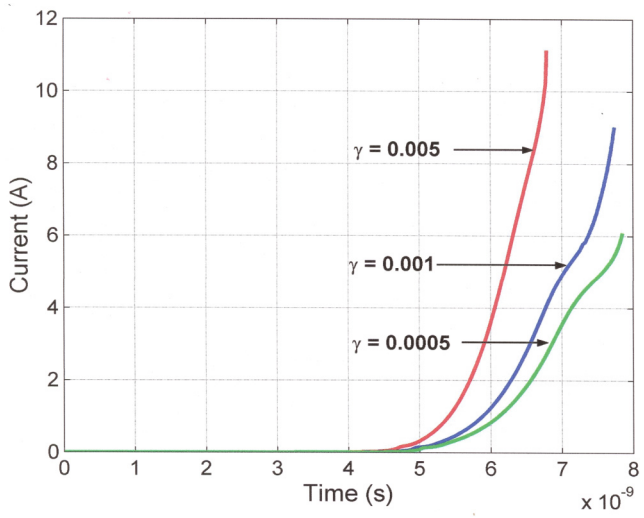

Fig. (12). Conductive current versus time for three different photoemission coefficients in a parallel plate of 1 cm apart at an applied voltage of 5600 V.

Fig. (**13**) shows the one-dimensional neutral gas temperature distribution along the symmetry axis for three different photoemission coefficients. The higher it is, the more heating is experienced throughout the discharge. The photoemission plays a major role in the heating of the cathode as the difference in temperature between different levels of photoemission is largest in that region. Furthermore, according to theory, local constrictions due to non-uniformities of the neutral gas are expected to form, as shown by the large temperature gradients that exist all along the symmetry axis of the discharge. Fig. (**13**) shows that the cathode emission properties, such as photoemission, are vital to the heating of the neutral gas. The dynamics of the discharge is shown to be quite extreme, since within a few nanoseconds, the temperature of the neutral gas is raised from 300-700 ^{o}K.

Photoionization Model in Air

The physical model of photoionization in air assumes that UV radiation originates from the nitrogen molecules, $N_2(C_3 5u)$ in singlet excited states b $^1\Pi$, b$'$ $^1\Sigma_u^+$, and c$_4$ $^1\Sigma_u^+$ in the wavelength range of 980-1025 Å, which is then absorbed mainly by oxygen and leads to photoionization [83]. The wavelength of 1025 Å corresponds to the ionization threshold of oxygen. It is worth noting that the rate of photoionization in air depends on the oxygen fraction and tends to zero when the oxygen fraction also reduces to zero [84]. In the photoionization model, two elemental volumes dV_1 and dV_2 are considered, with the distance between these elemental volumes being r. The rate of photoionization is then calculated as the number of electron-positive ion pairs generated every second over each cubic centimetre from the radiation of an elemental volume dV_2 to the elemental volume dV_1 as shown in Fig. (**14**) by:

$$S_{ph}(dV_1, dV_2) = \frac{R(dV_2) f(r)}{4\pi\, r^2} dV_2 \tag{23}$$

where the function $f(r)/4\pi r^2$ is the probability of photon absorption at the distance *r* from the emission point, $R(dV_2)$ is the integral intensity of emission of the source volume dV_2 (the number of photons produced per second per cm^3) to the receiving acceptor volume dV_1 and it is proportional to the rate of collisional ionization frequency α as follows:

$$R(dV_2) = \frac{P_q}{P + P_q} \xi \omega N_e W_e \tag{24}$$

$$R(dV_2) = \frac{P_q}{P + P_q} \alpha \phi N_e W_e \tag{25}$$

where P [= 760 Torr] is the gas pressure, P_q is the quenching pressure of the radiative states (for ambient air, P_q = 30 Torr [85]), ξ is the probability of ionization of a molecule by photon absorption which is a dimensionless factor, ω is the coefficient of excitation of the radiating states of molecules by electron impact, and α is the ionization coefficient. The factor $P_q/(P+P_q)$ is the quenching factor, and reflects the concurrence between radiative and collisional quenching of emitting molecular states [83]. The function f(r) is calculated as follows:

$$f(r) = \frac{\exp^{-Po_2 r \xi_{\min}} - \exp^{-Po_2 r \xi_{\max}}}{r \log(\xi_{\max} / \xi_{\min})} \tag{26}$$

where ξ_{min} = 0.035 and ξ_{max} = 2 cm^{-1} $Torr^{-1}$ are the minimum and maximum values of the coefficients of absorption by oxygen of ionizing radiation in the wavelength domain 980-1025 Å, with P_{O2} = 150 Torr [86].

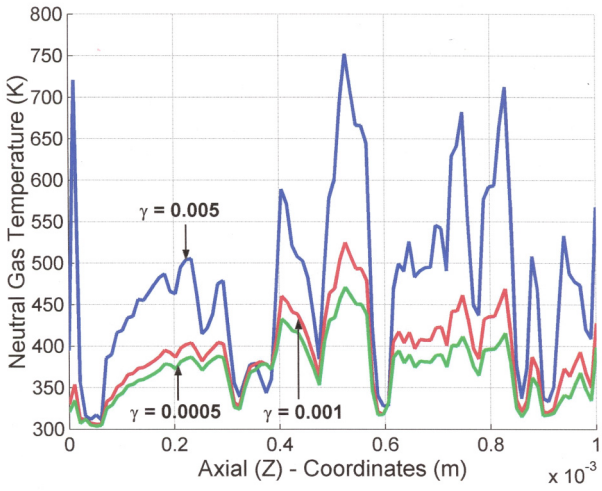

Fig. (13). Neutral gas temperature along the axial coordinates for three different photoemission coefficients in a parallel plate of 1 cm apart at an applied voltage of 5600 V.

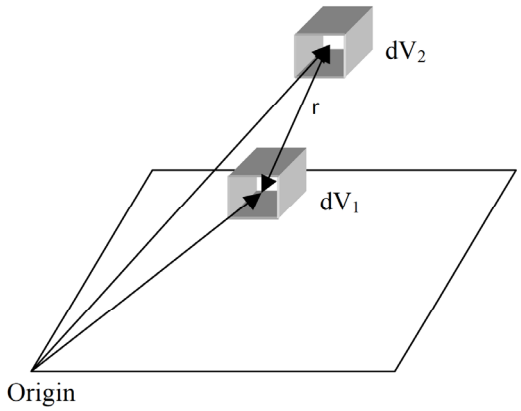

Fig. (14). Photoionization at the elemental volume dV_1 due to photon emission from volume dV_2.

The absorption coefficient Ψ is the number of photo-ions generated in a layer of unit thickness at distant r from the radiation source, per unit of solid angle, per one ionizing collision in the discharge, at unit pressure. Experimental calculations of the absorption coefficient Ψ in dry atmospheric air have been reported [87]. The absorption coefficient Ψ is calculated according to the following formula:

$$\Psi = \frac{f(r)P_q\phi}{4\pi(P+P_q)P} \tag{27}$$

For the experimental measurements to be approximately identical to the experimental ones in [87], the factor $\varphi = \xi\omega/\alpha$ is calculated by the author to be equal to 0.015. This figure should be contrasted with that of Hallac *et al.,* [88, 89], where the dimensionless factor φ is taken equal to 0.2, following the experimental results of Penney and Hummert's [90] at low pressures. The latter neglect the effect of the radiating states at high pressures.

The photoionization model is no longer valid at (Pd) values of 760 Torr cm and higher therefore, for the atmospheric discharge analyzed in this paper; the photoionization phenomenon has an effect up to a distance of approximately 1 cm or less. The absorption coefficient Ψ becomes negligible to a value of the order of 10^{-10} $Torr^{-1}$ cm^{-1} at Pd = 760 Torr cm, thereby reducing the numerical calculations considerably in long gaps. To simplify further the number of calculations performed, a coarser secondary grid is generated and photoionization values for a coarser grid are interpolated between two meshes.

Conductive Current Model

The total conductive current I during the evolution of the discharge is found by calculating the contribution of each element to the conductive current by multiplying $eN_s\mathbf{W_s}$ by the volume of each element dV. Therefore the equation is as follows:

$$I = \frac{1}{V_a}\int_V E_l . J_s dV \tag{28}$$

where V_a is the applied discharge voltage and E_l is the Laplacian field.

Displacement Current Model

In order to calculate the displacement current, there are two distinct methods [91]. In the first method one calculates the displacement current using the equation:

$$I_d = C_g \frac{dV}{dt} \tag{29}$$

In the case of an AC supply, the input voltage is $V=V_o\cos(\omega t)$, and the current is found to be:

$$I_d = -C_g \omega V_o \sin(\omega t) \tag{30}$$

Now to calculate C_g, one can calculate the total charge reaching the electrode and divide by the maximum applied voltage value of V_o.

The total charge reaching the electrode can be calculated by measuring the incoming electron and ion fluxes towards the electrodes [92], according to the general equation:

$$\frac{\partial \sigma_s}{\partial t} = \Gamma_s . \hat{n} \tag{31}$$

where Γ_s is the charge flux vector, $\hat{n}$ is the outward normal vector on the boundary of the dielectric and σ_s is the charge density which when multiplied by the area of the electrodes, will give the total amount of charges moving from the microplasma into the electrodes.

The second method calculates the displacement current using the equation of Morrow and Sato [93] as follows:

$$I_d = \frac{\varepsilon_o}{V}\int_{Vol} \frac{\partial E_l}{\partial t} E_l dVol \tag{32}$$

Since the applied voltage is given by:

$$V = V_o \cos(\omega t) \tag{33}$$

one can calculate the Laplacian electric field E_l by:

$$E_l = E_\phi \cos(\omega t) \tag{34}$$

Substituting (34) into equation (32), gives:

$$I_d = \frac{\varepsilon_o}{V_o \cos(\omega t)}\int_{Vol} \frac{\partial (E_\phi \cos(\omega t))}{\partial t} E_\phi \cos(\omega t) dVol \tag{35}$$

which simplifies to:

$$I_d = -\frac{\varepsilon_o \omega \sin(\omega t)}{V_o}\int_{Vol} E_\phi E_\phi dVol \tag{36}$$

If one compares the two expressions for the displacement current, one can derive a formula for the gap capacitance:

$$C_g = -\frac{\varepsilon_o}{V_o^2}\int_{Vol} E_\phi E_\phi dVol \tag{37}$$

External Current Model

Generally, if one wishes to calculate the external current in a discharge in which metallic electrodes are covered by dielectrics, the external current is expected to solely be the displacement current, since no net charge flows between the dielectric medium and the electrode metallic plate.

Dielectric Boundary Conditions

To calculate the voltages on the boundary air-dielectric medium, Gauss theorem can be used, taking into consideration the surface charge accumulated on the dielectrics together with the charge sources included [92]:

$$\hat{n}.\nabla V - \varepsilon_r \hat{n}.\nabla V_D = \frac{e}{\varepsilon_o}(\sigma_{ion} - \sigma_e) \quad (38)$$

$$\hat{n}\,x(\nabla V - \nabla V_D) = 0 \quad (39)$$

where σ_e is the electron surface charge density, σ_{ion} is the ion surface charge density both for positive and negative ions, V_D is the voltage on the dielectric medium, with ε_o and ε_r being the permittivity of free space and relative permittivity, respectively.

Fluid Model Results

In a recent work, the authors have simulated a DC microplasma discharge (CBL) using the suggested fluid model and studied the formation of the avalanche, the primary streamer, the secondary streamer, the accumulation of charges on the cathode and the radial expansion of the plasma towards the outer boundaries of the discharge in ambient atmospheric air. In this paper, the authors have observed electron densities of the order of 1 x 10^{14} cm^{-3}, temperatures increases from ambient of 300 ^oK up to 450 ^oK and conductive currents of 11 A. Regarding the boundary conditions, the dielectric boundary conditions were used from equations (38) and (39) and for secondary processes, photoionization phenomena in ambient air was also included as described by equations (23) to (27).

The microplasma configuration consists of a DC source voltage of 11.2 kV applied between two metallic parallel plates 4 mm apart. Two rectangular blocks of dielectric medium of relative permittivity 8 having a 1 mm thickness each, are attached to both the cathode and anode metallic electrodes, leaving the remaining 2 mm for the atmospheric barrier air discharge to develop.

At the start of the simulation, an initial electron is released close to the cathode and the electron, in the presence of the uniform electric field, advances towards the anode, ionizing the ambient air and forming the avalanche effect. After 4 ns, the avalanche reaches the anode dielectric, and charges continue to accumulate there for subsequent avalanches, until a significant electric field is formed able to change the Laplacian electric field. Thereafter, a primary positive streamer is formed and travels from the anode towards the cathode. The propagation of the primary streamer towards the cathode is aided by subsequent avalanches originating from the cathode. When the primary streamer hits the cathode dielectric at around t = 9 ns, the charges of the streamer are accumulated on the dielectric cathode. At t = 12 ns, a secondary streamer is formed at the anode travelling towards the cathode. The secondary streamer, while traversing towards the cathode, also expands radially towards the outer boundaries of the discharge, covering the whole cathode dielectric surface with charges. The accumulation of these charges at the electrodes significantly reduces the electric field into the inter-electrode gap and increases the electric field into the dielectric coatings. This leaves only the existence of radial electric field gradients along the cathode dielectric surface to push the discharge outwards towards the outer boundaries.

Fig. (**15**) shows the total conductive current with respect to time as calculated by equation (28). The microplasma discharge is simulated for duration of 0.32 μs. The current during the first 25 ns, which includes the formation of the avalanche effect, the primary streamer and the secondary streamer is very low, however it increases significantly with the arrival of the secondary streamer at the cathode. This marks the initiation of the redistribution of the charge at the cathode dielectric, where it increases the conductive current rapidly to 11 A. When the secondary streamer head is completely absorbed, the conductive current is stabilized, and thereafter the current tends to decrease. However due to the increased net charge densities and electric field formed at the cathode dielectric, the heating of the gas increases, and the neutral gas density expands radially outwards. This results in a neutral gas density reduction and since the ionization and attachment processes within the discharge are exponentially dependent upon the neutral gas density, the small decrease of the neutral gas density increases the total conductive current in the discharge.

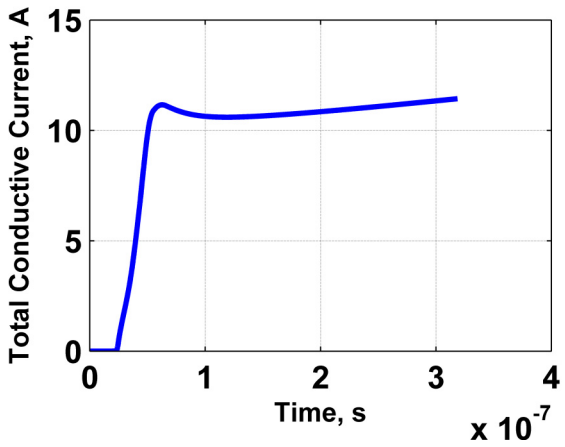

Fig. (15). Plot of the total conductive current versus time.

Fig. (**16**) shows the one-dimensional plot of the neutral gas temperature at three different instances of time. It is shown that there is a significant increase in the temperature of the discharge, rising from an initial ambient temperature of 300 ^oK, to a maximum value of approximately 450 ^oK. This shows that heating effects are important, and that their inclusion in the analysis of DC atmospheric-pressure air microplasmas is necessary. Similarly to other measured variables, the temperature rise, which is caused solely from the Joule heating effect, follows a striations pattern, in accordance to experimental and numerical results [9, 12]. As expected, most of the heating occurs along and close to the symmetry axis, where most of the discharge activity takes place. However, the plot shows that significant heating also occurs radially outwards from the symmetry axis. This rise in temperature is expected to cause movement of the neutral gas density, generating compression and rarefraction waves, which disturb the initial uniform neutral gas density, and therefore the ionisation processes within the air gap.

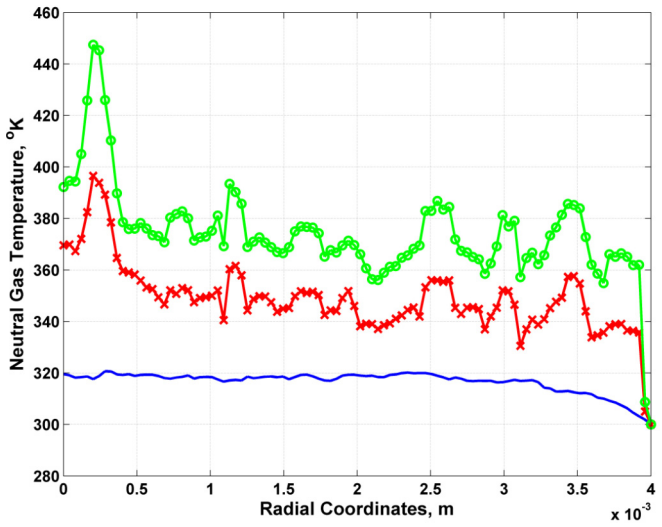

Fig. (16). Plot of the neutral gas temperature history along the radial coordinates at an axial distance of 1.2 mm from the cathode (t = 0.2938 μs (blue solid line), 0.3263 μs (red crossed line) and 0.5045 μs (green circled line).

Fig. (**17**) shows the two-dimensional neutral gas temperature distribution at time t = 0.3263 μs. It is shown that most of the heating within the microplasma occurs along the symmetry axis where most of the activity takes place. The column of heated air extends to a radial distance of 0.2 mm, and the temperature is raised approximately 120 °K. It is also shown that striations occur between the anode and the cathode. Along the dielectric electrodes, the temperature is larger than in the inter-electrode gap, but smaller than that along the symmetry axis.

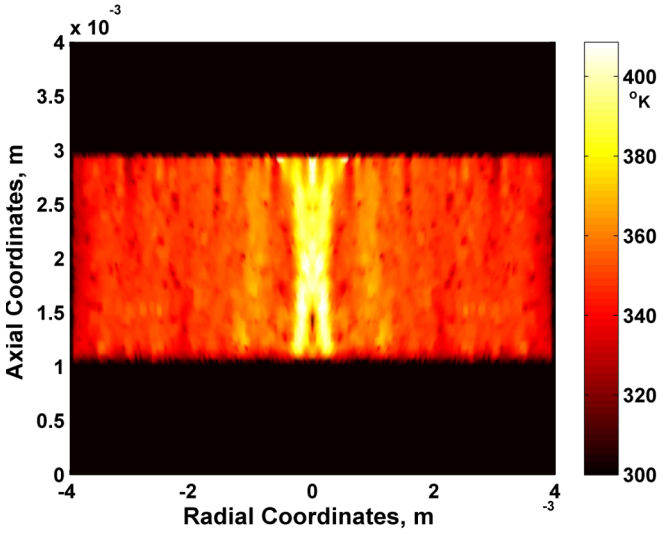

Fig. (17). Plot of the two-dimensional cylindrical axisymmetric neutral gas temperature at time t = 0.3263 μs.

Fig. (**18**) shows the two-dimensional axial electric field distribution at time t = 11.8 ns. In the center of the discharge, there exists a cathode fall, negative glow, positive column and anode regions, similar to those of a normal glow discharge. At a radial distance of 1.5 mm, a secondary streamer forms which travels from the anode towards the cathode. The secondary streamer is shown to extend radially up to the outer boundaries of the discharge and at later stages, when it hits the cathode, the sheath region spreads throughout the cathode dielectric surface.

Fig. (**19**) shows the one-dimensional plot of the electron density along the radial coordinates at times t = 0.2938 and 0.3263 μs at an axial distance of 1 mm. The electron density is shown to be of the order of 10^{19} m^{-3}, and it is shown to vary along the radial axis. At a time of t = 0.2938 μs, the electron densities at the cathode dielectric are approximately 4 x 10^{19} m^{-3} and vary fairly smoothly along the radial direction. After some time, the average value of the electron density reduces to values of approximately 2 x 10^{19} m^{-3}. Even though the average value for the electron density is nearly halved, the electron density varies abruptly along the radial directions forming axial and radial electric field spots.

Kinetic Models

In kinetic models, the particle velocity distribution function is analyzed at each position in the plasma domain by solving the Maxwell Boltzmann equation, rendering the Maxwell Boltzmann velocity distribution assumption unnecessary [94]. Generally, kinetic models are much more computationally intensive than fluid models. In low pressure collissionless plasmas, a kinetic description must be used since fluid models are no longer valid.

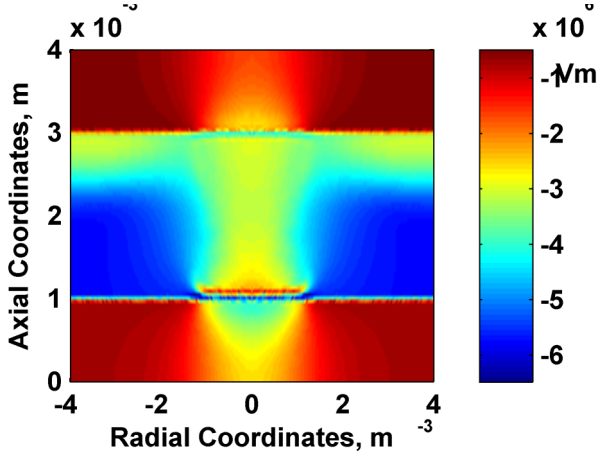

Fig. (18). Plot of the two-dimensional axial electric field distribution at time t = 11.8 ns.

Examples of kinetic modeling include the Monte Carlo (MC) simulations [95] which are mathematically simple, and accurately account for the non-equilibrium behaviour of the plasma species. In the MC simulations, the trajectories of individual particles are described by Newton's laws, and the collisions are treated as random, therefore a large number of individual particles are simulated such that statistically valid results are reached. However, MC simulations are very time-consuming, especially for slow-moving particles. Moreover, a MC model in itself is not consistent, because it requires a certain electric field distribution as an input value. This problem is overcome by the Particle In Cell-Monte Carlo (PIC-MC) method [96], which couples MC simulations for the behaviour of ions and electrons, to the Poisson equation for a self-consistent electric field distribution, which includes the kinetic description of the trajectories of a large number of individual particles. However, this makes this modelling approach computationally even more time-consuming. In plasma physics applications, the method amounts to

following the trajectories of charged particles in self-consistent electromagnetic (or electrostatic) fields computed on a fixed mesh.

In the paper of Takao *et al.,* [97], the microplasma characteristics of an RFIC microplasma have been investigated using PIC-MC calculations (kinetic model) and a fluid model (collisional model) in a two-dimensional axisymmetric geometry at pressures of 370-770 mTorr and at a frequency of 450 MHz. It has been shown that a thick sheath structure is formed in which the electron energy distribution function (EEDF) is non-Maxwellian, thereby providing different results from those used in the fluid model. Furthermore, the pressure is shown to exhibit different dependence between the two models, implying that even at high pressures where the electron collision frequency is less than the driving RF frequency, non-collisional effects may exist.

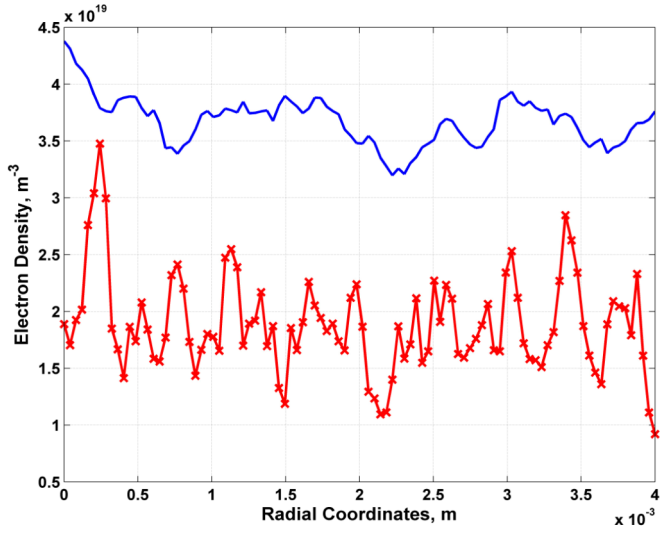

Fig. (19). Plot of the electron density history along the radial coordinates at an axial distance of 1.2 mm from the cathode (t = 0.2938 μs (blue solid line), 0.3263 μs (red crossed line).

The time-averaged electron density in a miniature RFIC microplasma source based on the collisional model and the kinetic model are calculated and compared in [97]. The peak value of the electron density in the kinetic model is found to be 8.2 x 10^{10} cm^{-3} instead of 7.8 x 10^{10} cm^{-3}, in the collisional model.

Electron and ion kinetics in various microplasmas are analyzed by Iza *et al.,* [34] using one and two-dimensional PIC-MC simulations. The open source codes of XOOPIC [98] and XPDP1 [99] and the source code developed by Iza and co-workers of APPS2 [100, 101] were used to study various microplasmas. Due to the high computational cost of the PIC-MC simulations, the number of species and their reactions were limited, thereby including electrons and single charged ions (Ar^+, He^+, Ne^+, and Xe^+) in the models, with the neutral gas temperature assuming to be uniformly distributed at ambient values. The processes included in the simulations were the elastic, excitation, and ionisation electron-neutral collisions, whereas Coulomb collisions were excluded due to computational constrains. According to Iza *et al*., the electron/electron collisions must be included when the energy transfer in electron/electron collisions is similar to those of electron/neutral collisions, whereas Coulomb collisions should be considered at microdischarges with densities above 10^{14} cm^{-3}.

Hybrid Models

Since each method has its advantages and disadvantages, one can also use hybrid models [102] i.e. use PIC-MC methods for regions where the plasma species are not in equilibrium with the electric field, and fluid models for slower plasma species, where the velocity profile of the particles follows a Maxwellian velocity distribution. Hong *et al.,* [103] compared simulation of microplasmas using a fluid model and a PIC-MC model. The kinetics of He discharges at 760 Torr and Ne/Xe DBD discharges at 300 Torr at various geometries and driving currents are analyzed. It is found that near the sheath region, the EEDF exhibits a non-equilibrium behavior, whereas in the rest of the discharge fluid models are adequate to simulate accurately the behaviour of the discharge. This is expected since the sheath region is associated with high electric fields that force the fast moving electrons outside the Maxwellian distribution regime.

Molecular Dynamics Models (MD)

In case where one needs to study plasma wall interactions, one can revert to molecular dynamics simulations for example to study thin film deposition processes. Molecular dynamics simulations [104] utilize Newton's laws using the interatomic interaction potentials between all species to analyze the above interactions, however they are computationally very time consuming.

EXPERIMENTAL ANALYSIS

For the experimental analysis of microplasmas, Optical Emission Spectroscopy (OES), Cross-Correlation Spectroscopy (CCS), Laser Interferometry (LI), Diode Laser Absorption (DLA), Laser Induced Fluorescence (LIF), Molecular Beam Mass Spectrometry (MBMS), Langmuir probes and Thomson scattering are used to provide spatiotemporal evolutions of the different species involved.

Optical Emission Spectroscopy (OES)

Generally, to characterize the plasma dynamics experimentally, OES is widely used to obtain spatiotemporal evolutions of the plasma parameters. OES of plasmas can be measured through a sapphire tube connected with an Intensified Charge Coupled Device (ICCD) camera with subnanosecond shuttering speeds, a spectrometer with an instrumental resolution of 0.1 nm and a data acquisition computer to record the measurements.

Electron densities can be measured using the OES based on the Stark broadening width of the H_β line, with hydrogen possibly added to the microplasma to obtain a detectable level of H_β emission intensity, and from the N_2 first and second positive band systems. The electron temperature can also be measured from the N_2 first and second positive band systems.

The characteristics of the electron energy in microwave atmospheric-pressure argon microplasma are investigated by a spatially resolved OES technique in a microstrip split-ring resonator. By adding a tiny amount of xenon (< 1 ppm) as

tracer gas into the argon discharge, spatial distributions of two electron groups, one with electron energy of 8.3 eV and one with electron energy of 11.5 eV, have been identified, showing spatial non-uniformity [105]. In a work by Mariotti *et al.,* [106], OES has been used to obtain gas and electron temperature distributions.

Spatially resolved temperature measurements at normal pressures in microplasmas have been conducted by Staack *et al.,* [107, 108] and Laux *et al.,* [109, 110]. The vibrational and rotational temperatures of DC normal glow discharges were measured by Stack *et al.,* using the emission spectra of the second positive system of N_2 with spectroscopic measurements from the discharges. The second positive system of bands gaps has been used several times for temperature measurements of plasma systems. The temperatures observed are in close agreement with the results obtained by Papadakis *et al.,* [111], which showed an increased temperature rise near the cathode and anode regions, with intermediate temperatures within the inter-electrode gap. Temperatures recorded in MHCD using OES were found to be in the range from 1700-2000 ^oK [112]. In atmospheric-pressure discharges, the rotational and vibrational temperatures varied from the range of 600 to above 2000 ^oK over different discharge currents and voltages in the normal glow operating regime. Rotational, vibrational and excitational temperatures of the neutral gas can also be measured using the emission spectrum of the OH A-X transition around 300 nm.

In the work by Zhu *et al.,* [113], OES is used to measure the neutral gas temperature, and the electron density and temperature of a microwave excited microstrip split-ring resonator in argon microplasma near atmospheric-pressure. With less than 100 ppm of water in the plasma, the gas temperature is calculated by the rotational temperature of the hydroxyl molecule ($A^2\Sigma^+$, v = 0), whereas the electron density is measured by the Stark broadening of the hydrogen Balmer β (H_β) line. Thereafter, the electron temperature is estimated from the measured excitation temperature of argon 4p and 5p levels using a collisional–radiative model. The above parameters were not found to increase as the gap resonator length was reduced, but with the increase in power the above parameters, especially the electron density, were found not to increase significantly.

Zhu *et al.,* have calculated the electron density for different microplasma gaps of 67, 80, and 115 μm. It is found that the electron density is of the order of 1.1 x 10^{14} cm^{-3}, and reduces as the gap is increased, with the electron density reaching values of 5.5 x 10^{13} cm^{-3}. The decrease is attributed to the larger volume to surface ratio of the discharge which makes surface processes less effective and secondly due to the reduction of the electron temperature and therefore of the ionization processes in the microplasma discharge.

Since the dominant heating mechanisms in microwave excited atmospheric-pressure argon microplasmas are the elastic collisions between electrons and atoms, the rotational temperature is used to calculate the neutral gas temperature of the microplasma. This is because the typical lifetime of such species, of the order of approximately 10-100 ns, is much longer than the rotational to translational energy transfer characteristic time which is approximately between 0.1-1 ns. Zhu *et al.,* [113] also measured the rotational temperature along the microplasma split-ring resonator at three different gaps of 67, 80 and 115 μm. The rotational temperature reaches values of 580 ^oK and reduces to 525 ^oK at a gap of 80 μm, and reduces further to a value of 515 ^oK at a distance of 115 μm. Since the electron density decreases with the increase in the gap distance, it is expected that the neutral gas temperature will also decrease.

Cross-Correlation Spectroscopy (CCS)

Another method used to obtain spatiotemporal evolution in microplasmas is the CCS [114-117]. This is an OES method that uses the time-correlated single photon counting technique to provide spatiotemporal evolutions in scales smaller than mm in space and ns in time [118]. The CCS utilizes the luminosity of the 0–0 transitions of the second positive system (λ = 337.1 nm) and the first negative system (λ = 391.5 nm) of molecular nitrogen to produce the spatiotemporal evolutions. The CCS measures repetitively light emissions and uses statistical averaging of the cross-correlation function of two optical signals that both originate from the discharge light pulse itself. The two optical signals are the main signal, which is a spatially and spectrally resolved single photon, and the synchronization signal. By using the time delay between the two signals, relative time information is calculated for each photon [119, 120].

Laser Induced Fluorescence (LIF)

LIF uses the optical emission from molecules which have been excited at higher energy levels by absorption of the electromagnetic radiation. In LIF, a pulsed-laser beam is used to selectively excite the plasma atoms causing them to emit a pulse of fluorescent light at a characteristic wavelength. LIF measurements using nanosecond laser in plasmas have been conducted by Nakane *et al.,* [121] and Sdorra and Niemax [122]. In the work of Margetica *et al.,* [123], they use femtosecond LIF to study the expansion of a femtosecond laser produced microplasma at different pressures.

LIF when compared with emission techniques, has better spatial and temporal resolution and a longer observation time due to the fact that atoms or ions can be excited even after the emission has ceased [123]. A high signal-to-noise ratio exists which allows LIF to have very short observation times during experimental measurements.

Two-Photon Laser Induced Fluorescence (LIF) has been used to study the density of atoms in nitrogen plasma jets [124] and to provide spatial profiles of absolutely calibrated atomic oxygen densities [125, 126]. Consequently, the two-dimensional distribution of the ground state absolute densities of atomic oxygen of a planar atmospheric-pressure plasma jet for a helium flux of 2 m^3 h^{-1}, 0.5 vol% O_2 admixture at a RF power of 150 W was analyzed. The initial atomic oxygen ground state density at the nozzle is measured to be 1×10^{16} cm^{-3}, and as expected reduces significantly as one moves away from the nozzle. It is also shown that at a distance of 10 cm, the density of the atomic oxygen reduces significantly, however it is still within approximately 1% of the initial value at the nozzle. In a further work, Tachibana [127] has used LIF to study the N_2^+ ions in a microplasma jet.

Molecular Beam Mass Spectrometry (MBMS)

MBMS has recently been used to determine the ionic composition of negative and positive ions in microplasmas [128, 129]. A typical MBMS instrument combines a time-of-flight mass spectrometer with single-photon, vacuum ultraviolet photoionization and a quadrupole mass spectrometer with electron-impact ionization. The single-photon near threshold ionization allows a way to reduce the formation of fragment ions, while at the same time identifying the different species by their ionization [130].

MBMS has been used to study the nucleation of particles in inductive microplasmas, which is the transition phase between individual small molecules to macromolecules. One of the major advantages of MBMS is its ability to study a large number of different species which usually exist in a microplasma discharge [131].

Diode Laser Absorption (DLA)

In the work of Miura and Hopwood [132, 133], spatially resolved DLA, by using the Ar 801.4 nm transition (1s5-2p8), was used to study a 900 MHz microstrip split-ring resonator microplasma in argon. Gas temperatures and the Ar 1s5 line-integrated densities were obtained from the atomic absorption lineshape at operating pressures of 100-760 Torr. The laser is focused at a 30 μm spot, and by translating the laser path using a xyz microdrive, spatial distributions of the gas temperature were obtained. It was observed that at ambient pressures, the core temperature of the microplasma was approximately 850 ^{o}K over an area of 0.2 mm wide and it is suddenly reduced to ambient temperature at the edge of the discharge. At lower pressure, reduced gas temperatures were observed and the spatial profiles were more diffused.

Laser Interferometry (LI)

LI is used for the spatiotemporal evolution of the electron density in microplasmas. According to Harilal *et al.,* [134], electron plasma densities can be measured using LI techniques where the variation of the refractive index of the medium is used to calculate the various plasma parameters. Different methods can be the beam-deflection angle measurement (shadowgraphy) or the phase measurement (interferometry). In the case of phase measurements, two beams propagate on separate paths and recombine at a later stage and depending on the phase shift of the two beams, the plasma parameters are calculated. In the case of the shadowgraphy, a light probe is scanned through the plasma and a photographic camera, such as a plate or a charged coupled device camera, is utilized to record the data. Some of the typical amplitude interferometers used are the Sagnac, Mach Zehnder, Michelson and Nomarski interferometers.

Tachibana [127] has measured the electron density radial profile of a microplasma jet at a distance of 1 mm from the nozzle exit and the maximum electron density was found to be of the order of $2.5x10^{12}$ cm^{-3} at a current of 120 mA when atmospheric-pressure He gas was fed at a flow rate of 6 L/min. The spatiotemporal distribution of the electron density and the refractive index of a microplasma jet in air and helium were also measured by Bukin *et al.,* [135] using LI at a precision of 1.5 μm using a femtosecond laser.

Other Techniques

For the calculation of the electron density, other techniques are used such as Langmuir probes, microwave interferometry, and Thomson scattering. In the density range from 10^{15}-10^{18} cm^{-3}, the Stark broadening of visible spectral lines is also used.

Finally, general microplasma parameters, such as electric current, voltage, electrode temperatures and power dissipation can also be measured using standard laboratory equipment.

CONSTRUCTION OF MICROPLASMAS

To analyze the surface structures formed, visualisation tools such as Scanning Electron Microscopes (SEM) and Tunnelling Electron Microscopes (TEM) can be used. Experimental methods used for the micromachining of the microplasma devices are Focused Ion Beam (FIB) [136], photolithography, plasma etching, plasma deposition and excimer laser techniques.

Since there are various methods of constructing microplasmas, one example on how to construct a metal-dielectric-metal sandwich structure with inverted square pyramidal hollow cathode from the work of Wen *et al.,* [137], using a novel maskless plasma etching system, is provided. The dielectric chosen was polyimide due its very good overall electrical, mechanical, thermal and other properties. Metal nickel was chosen to be used as electrode material and etch mask for the polyimide due to low cost, high melting points and low sputtering yields. The length of the squared base is 100 μm^2 and 70 μm in depth, with the thickness of metal nickel and polyimide film being 200 nm and 8-10 μm, respectively.

In the construction of inverted square pyramidal hollow cathode microplasmas, 12 different steps are used. The microplasma is formed by anisotropic wet etch. First, a p-type-100 orientation Si wafer is thermally grown with silicon dioxide ($Si0_2$) on both sides. Next, the $Si0_2$ is patterned as a mask layer of Si by reactive ion etching, and the inverted hollow pyramid is formed by anisotropic wet etching in 30% KOH at 70°C with $Si0_2$ as a mask, which is subsequently removed in a buffered oxide etch. Thereafter, a Ni film of 200 nm is sputtered on the wafer to be used as cathode. By using spin coating twice, the polyimide attaches on the device. The polyimide then goes a high temperature cure according to a series of controlled ramps and dwells in a programmable convection oven, in an attempt to optimize its electrical and mechanical properties. Thereafter, a liftoff process based on image reversal resist (ARU4030) is used to pattern the anode Ni as an etching mask of polyimide.

By utilizing a SEM or a TEM one has the visual means to construct and inspect the construction of microplasmas, which can be used especially for the air gap region, to study its uniformity, surface roughness, etching depth and quality and accurate air gap width, upon which the microplasmas' stability and lifetime operation primarily depend on.

DISCUSSION

In this paper, a general overview of microplasmas is conducted. Firstly, the various applications of microplasmas such as photonic devices, plasma cathodes, remediation of

VOC's, and many others have been discussed. The different configurations of microplasma devices have been reviewed, as well as the different experimental and numerical methods to analyze these microplasmas.

Undoubtedly, in the future new microplasma devices and configurations are expected to be developed. Microplasmas are used in some applications due to their unique ability to generate stable glow discharges from μm to mm scale with energetic high density electrons in the presence of a rather unheated neutral gas. In many cases, positive current-voltage characteristics are observed which facilitates the parallel operation of these microplasmas without the need for ballast resistors.

Very little work has been conducted regarding the plasma-wall interactions, such as sputtering effects and this is due to the complexity of the physical processes involved, as well as the large computational resources necessary to analyze such phenomena.

As far as the different microplasma configurations are concerned, the CBL microplasma is an efficient source of excimer radiation and the parallel operation of such devices is permitted without the need for any ballast resistors. However, the lifetime expectancy of these microplasmas is of the order of a few hours. DBD microplasmas have rather longer operational times and can be used as ionization sources. CPED microplasmas exhibit the capillary jet mode that suppresses the glow to arc transition and are used in the display, semiconductor, storage disk and optical communications industries, as well as plasma sources. Their lifetimes are short, typically hundreds of microseconds. The MHCD microplasmas can be utilized as plasma cathodes and excimer emitters and can be operated in parallel without the use of any ballast resistors, with a lifetime operation of a few hours.

The ISP microplasmas can also be used as plasma cathodes and photonic devices and exhibit hundreds of hours of stable operation. SCSC microplasmas are used as UV radiation sources and arrays of microplasmas as large as 25 x 25 pixels have been constructed operating in the abnormal glow discharge regime. RFIC microplasmas with an increase in the surface to volume ratios, are incapable of producing large charge particle densities. Even though they work better at VHF and UHF frequencies, their frequency of operation is limited, whereas lifetime operation is not an issue due to the almost non-existence sputtering effect due to the parallel electric field that exists on the cathode. RFCC microplasmas are able to operate at high pressures however the normal electric field at the walls increases the sputtering effect and reduces their lifetime of operation. MS microplasmas are well suited for longer operational lifetimes due to the higher frequencies which minimize the ion sputtering effects on the electrodes.

For modelling purposes, one can use fluid models, or kinetic models, or combine both methods in a hybrid approach. It is common in microplasmas near high electric field regions, for the electron dynamics to be non-Maxwellian, thereby requiring the usage of a kinetic approach to analyze accurately the discharge dynamics. Since the kinetic approach is very computationally intensive, the hybrid approach remains the best solution. Since microplasmas exhibit high temperatures in the gas, it is useful to include the neutral gas temperature effects by solving the Navier-Stokes equations together with the charged particle dynamics and Poisson's equations.

For experimental diagnostics of microplasmas, the most widely used methods are OES and LIF. LIF has better spatial and temporal resolution and a longer observation time than OES due to the fact that atoms or ions can be excited even after the emission has ceased.

As far as high pressure microplasma in air is concerned, it has been shown that the future lies in the utilization of (a) microstrip technology and (b) DBD. Examples of such technology were (a) the split-ring resonator at 895 MHz at an input power of 3 W, (b) the microstrip technology at 2.45 GHz at an input power of 1 W, and (c) the DBD from several kHz to greater than 20 MHz at an input power of 0.25 W. The above configurations have proven to be the only methods capable of producing stable glow discharges in high pressure air microplasmas, with a lifetime operation of more than a few days.

Finally, the main drawback of the microstrip technology is the large size of the devices, of the order of a few tens of millimetres. The way forward would be the construction of ambient air microplasmas with air gaps in the submillimeter scale and device sizes of the order of a few millimetres, with a long lifetime operation, at low power consumption and low costs, without the use of any flow gases. This could be achieved by using much higher operating frequencies, thereby reducing the wavelength and enabling the construction of microplasma devices with sizes of a few millimetres. The use of a higher frequency would result in the more frequent reversal of the field within the air gap, which does not enable the ions to gain significant momentum before colliding with the dielectric walls, thereby reducing the ion sputtering effect and extending the lifetime operation of these microplasmas. The amount of power necessary to ignite and sustain the microplasma is expected to be considerably reduced due to the smaller air gaps used, paving the way for these microdevices to be incorporated in semiconductor microwave circuits.

ACKNOWLEDGEMENT

Part of this work has also been supported by the Contract of Association EURATOM-Hellenic Republic.

CONFLICT OF INTEREST

None declared.

REFERENCES

[1] Georghiou GE, Papadakis AP, Morrow R, Metaxas AC. Numerical modelling of gas discharges leading to plasma production. J Phys D: Appl Phys 2005; 38: R303-28.

[2] Foest R, Schmidt M, Becker K. Microplasmas, an emerging field of low-temperature plasma science and technology. Int J Mass Spectrom 2006; 248: 87-102.

[3] Becker KH, Schoenbach KH, Eden JG. Microplasmas and Applications. J Phys D: Appl Phys 2006; 39: R55-70.

[4] Tachibana K. Current status of microplasma research. IEEJ T Electr Electr Engineering 2006; 1: 145-55.

[5] Karanassios V. Microplasmas for chemical analysis: analytical tools or research toys?. Spectrochim Acta B 2004; 59: 909-28.

[6] Mariotti D, Sankaran RM. Microplasmas for nanomaterials synthesis. J Phys D: Appl Phys 2010; 43: 323001-1-21.

[7] Kong MG, Kroesen G, Morfill G, *et al*. Plasma medicine: an introductory review. New J Phys 2009; 11: 115012-1-35.

[8] New instrumentation and alternative plasma sources European winter conference on plasma spectrochemistry; Germany: Garmish-Pertenkirchen 2003; January 15.

[9] 1st International Workshop on Microplasmas. The new world of microplasmas. Kyoto University: Hyogo, Japan. February 2003.

[10] Hoboken NJ. 2nd International Workshop on Microplasmas. Stevens Institute of Technology. Hoboken: NJ, USA, 6-8 October 2004.

[11] 3rd International Workshop on Microplasmas. Greifswald Germany May 9-11 2006. Available at: http://www.inp-greifswald.de/iwm2006.nsf/index? OpenPage.

[12] 4th International Workshop on Microplasmas. Diagnostics of Microplasmas. Tainan, Taiwan 28-31 October 2007.

[13] 5th International Workshop on Microplasmas. Bochum, Germany, 21-23 March 2010.

[14] 6th International Workshop on Microplasmas. Paris, France, 3-6 April 2011.

[15] Blades MW, Karcus RK (Organizers). Miniaturization in analytical atomic spectrometry: we're behind the curve. Pittsburgh, New Orleans, USA.March 2002.

[16] Karanassios V (Organizer). Plasmas on a chip: microplasma devices. Winter Conference on Plasma Spectrochemistry. 2002 9th January.Scottsdale AZ, USA.

[17] Karanassios V (Organizer). Miniaturization and microplasmas. FACSS Conference . Providence, RI, USA 2002 October 17.

[18] Cluster Issue on Microplasmas. J Phys D: Appl Phys. Available at: http://iopscience.iop.org/0022-3727/41/19

[19] Wikipedia, Microplasmas. [Retrieved 2011 February]. Available at: http://en.wikipedia.org/wiki/Microplasma

[20] Gostev V, Dobrynin D. Medical microplasmatron. 3rd International Workshop on Microplasmas (IWM-2006). Greifswald, Germany 2006.

[21] Misyn FA, Gostev VA. Cold plasma application in eyelid phlegmon curing diagnostics and treatment of infectious diseases. Petrozavodsk, Russia 2000.

[22] Sankaran RM, Holunga D, Flagan RC, Giapis KP. Synthesis of blue luminescent Si nanoparticles using atmospheric-pressure microdischarges. Nano Lett 2005; 5: 537-41.

[23] Fridman G, Friedman G, Gutsol A, Shekhter AB, Vasilets VN, Fridman A. Applied plasma medicine. Plasma Process Polym 2008; 5(6): 503-33.

[24] Becker K, Koutsospyros A, Yin SM, *et al*. Environmental and biological applications of microplasmas. Plasma Phys Contr F 2005; 47: B513-23.

[25] Fateev A, Stamate E, Michelsen P. Ozone generation by micro-plasma devices: feasibility study. 28th ICPIG. Prague, Czech Republic, 15-20 July 2007.

[26] Ishii S. Microplasma as a New Science and Technology. IEEE Trans Fund Mater 2004; 124(1): 7-8.

[27] Yokoyama T, Hamada S, Ibuka S, Yasuoka K, Ishii S. Atmospheric dc discharges with miniature gas flow as microplasma generation method. J Phys D: Appl Phys 2005; 38: 1684-9.

[28] Stoffels E, Flikweert AJ, Stoffels WW, Kroesen GMW. Plasma needle: a non-destructive atmospheric plasma source for fine surface treatment of (bio)materials. Plasma Sources Sci Technol 2005; 11: 383-8.

[29] Moselhy M, Schoenbach KH. Excimer emission from cathode boundary layer discharges. J Appl Phys 2004; 95: 1642-9.

[30] Benilov MS. Comment on 'Self-organization in cathode boundary layer discharges in xenon' and 'Self-organization in cathode boundary layer microdischarges'. Plasma Sources Sci Technol 2007; 16: 422-5.

[31] Zhu W, Takano N, Schoenbach KH, *et al.* Direct current planar excimer source. J Phys D: Appl Phys 2007; 40: 3896-906.

[32] Takano N, Karl H, Schoenbach KH. Self-organization in cathode boundary layer discharges in xenon. Plasma Sources Sci Technol 2006; 15: S109-17.

[33] Schoenbach KH, Moselhy M, Shi W. Self-organization in cathode boundary layer microdischarges. Plasma Sources Sci Technol 2004; 13: 177-85.

[34] Iza F, Kim GJ, Lee SM, *et al*. Microplasmas: Sources, Particle Kinetics, and Biomedical Applications. Plasma Proces Polym 2008; 5: 322-44.

[35] Eijkel JCT, Stoeri H, Manz A. A molecular emission detector on a chip employing direct current microplasma. Anal Chem 1999; 71: 2600-6.

[36] Wright JA, Miller RA, Nazarov EG. Atmospheric Pressure Air Microplasma Ionization Source for Chemical Analysis Applications. MEMS 2006. Istanbul, Turkey, 22-26 January 2006.

[37] Iza F, Hopwood J. Rotational, vibrational, and excitation temperatures of microwave-frequency microplasma. IEEE Trans Plasma Sci 2004; 32: 498-504.

[38] Kogelschatz U. Applications of Microplasmas and Microreactor Technology. Contrib Plasma Phys 2007; 47(1-2): 80-8.

[39] Kunhardt EE, Becker K, Amorer L. Suppression of the glow-to-arc transition. Proceedings XII International Conference on Gas Discharges and Their Applications; Greifswald, Germany.

[40] Kunhardt EE. Generation of large-volume, atmospheric- pressure, non-equilibrium plasmas. IEEE Trans Plasma Sci 2000; 28: 189-200.

[41] Moskwinski L, Picatto PJ, Babko MS, *et al*. Al Surface Cleaning Using a Capillary Plasma Electrode Discharge (CPED). Plasma American Physical Society 55th Gaseous Electronic Conference. Minneapolis MN Meeting ID GEC02 15-18 October 2002.

[42] Panikov NS, Paduraru S, Crowe R, Ricatto PJ, Christodoulatos C, Becker K. Destruction of *Bacillus Subtilis* cells using an atmospheric-pressure capillary plasma electrode discharge. IEEE Trans Plasma Sci 2002; 30: 424-8.

[43] Foest R, Schmidt M, Becker K. Microplasmas, an emerging field of low-temperature plasma science and technology. Int J Mass Spectrom 2006; 248: 87-102.

[44] Shi W, Stark RH, Schoenbach KH. Parallel Operation of Microhollow Cathode Discharges. IEEE Trans Plasma Sci 1999; 27: 16-7.

[45] Meyer C, Heming R, Gurevich EL, *et al*. Radiofrequency driven and low cost fabricated microhollow cathode discharge for gaseous atomic emission spectrometry. J Anal At Spectrom 2011; 26: 505-10.

[46] Abdel-Aleam HM, Rolf B, Schoenbach KH. Direct Current Glow Discharges in Atmospheric Air. IEEE Trans Plasma Sci 2002; 30(1): 182-3.

[47] Schoenbach KH, Verhappen R, Tessnow T, Peterkin FE. Microhollow cathode discharges. Appl Phys Lett 1996; 68: 13-5.

[48] Alexeff I, Laroussi M. A steady-state one atmosphere uniform DC glow discharge plasma. Proceedings IEEE International Conference on Plasma Science; San Diego, CA, June 1999.

[49] Puech V. Microplasmas: physics and application to the production of singlet oxygen $0_2(\alpha^1\Delta_g)$. Eur Phys J Appl Phys 2007; 42: 17-23.

[50] Schoenbach KH. Microhollow Cathode Discharges. Laser Processing Consortium – FEL Users' Workshop. March 20, 2003, [Retrieved 2011 March] Available at: http://www.jlab.org/FEL/LPC/03lpc-schoenbach.pdf

[51] Park SJ. Stable Microplasmas in Air Generated With a Silicon Inverted Pyramid Plasma Cathode. IEEE Trans Plasma Sci 2005; 33: 570-1.

[52] Eden JG, Park SJ. Microcavity plasma devices and arrays: a new realm of plasma physics and photonic applications. Plasma Phys Contr F 2005; 47: B83-92.

[53] Eden JG, Park SJ, Ostrom NP, Chen KF. Recent advances in microcavity plasma devices and arrays: a versatile photonic platform. J Phys D: Appl Phys 2005; 38: 1644-8.

[54] Park SJ, Chen KF, Ostrom NP, Eden JG. 40 000 pixel arrays of ac-excited silicon microcavity plasma devices. Appl Phys Lett 2005; 86: 111501-1-3.

[55] Park SJ, Eden JG, Chen J, Liu C. Microdischarge devices with 10 x 30 micrometer square silicon cathode cavities: pd scaling and production of the XeO excimer. Appl Phys Lett 2004; 85: 4869-71.

[56] El-Habachi A, Schoenbach KH. Generation of intense excimer radiation from high-pressure hollow cathode discharges. Appl Phys Lett 1998; 73: 885-7.

[57] Sung-O K, Gary EJ. Arrays of Microplasma Devices Fabricated in Photodefinable Glass and Excited AC or DC by Interdigitated Electrodes. IEEE Photonics Technol Lett 2005; 17: 7: 1543-5.

[58] Kim SO, Eden JG. Arrays of Microplasma Devices Fabricated in Photodefinable Glass and Excited AC or DC by Interdigitated Electrodes. IEEE Photonic Technol Lett 2005; 17(7): 1543-1545.

[59] Park J, Henins I, Herrmann HW, Selwyn GS. Gas breakdown in an atmospheric pressure radio-frequency capacitive plasma source. J Appl Phys 2001; 89: 15-9.

[60] Surendra M, Graves DB. Capacitively coupled glow discharges at frequencies above 13.56 MHz. Appl Phys Lett 1991; 59: 2091-3.

[61] Hopwood J, Iza F, Coy S, Fenner DB. A microfabricated atmospheric-pressure microplasma source operating in air. J Phys D: Appl Phys 2005; 38: 1698-703.

[62] Liu BYH, Pui DYH. Equilibrium Bipolar Charge Distribution of Aerosols. J Colloid Interface Sci 1974; 49: 305-12.

[63] Xue J, Hopwood JA. Microplasma Trapping of Particles. IEEE Trans Plasma Sci 2007; 35(5): 1574-9.

[64] Hoskinson AR, Hopwood J, Bostrom NW, Crank JA, Harrison C. Low-power microwave-generated helium microplasma for molecular and atomic spectrometry. J Anal At Spectrom 2011; 26: 1258-64.

[65] Jaeho K, Kazuo T. 2.45 GHz microwave-excited atmospheric pressure air microplasmas based on microstrip technology. Appl Phys Lett 2005; 86: 191504-1-3.

[66] Gregorio J, Alves LL, Leroy O, Leprince P, Boisse-Laporte C. Microwave microplasma sources based on microstrip-like transmission lines. Eur Phys J D 2010; 60: 627-35.

[67] Bogaerts A, Bleecker KD, Georgieva V, Kolev I, Madani M, Neyts E. Computer Simulations for Processing Plasma. Plasma Proces Polym 2006; 3: 110-9.

[68] Morgan WL, Penetrante BMA. ELENDIF: A time-dependent Boltzmann solver for partially ionized plasmas. Comput Physical Commun 1990; 58: 127-52.

[69] BOLSIG 2011 CPAT [Retrieved 2011 March]. Available at: http://www.siglo-kinema.com/bolsig.htm

[70] BOLSIG+ 2011 CPAT [Retrieved 2011 March]. Available at: http://www.bolsig.laplace.univ-tlse.fr/

[71] Hagelaar GJM, Pitchford LC. Solving the Boltzmann equation to obtain electron transport coefficients and rate coefficients for fluid models. Plasma Sources Sci Technol 2005; 14: 722-33.

[72] Pitchford LC, ONeil SV, Rumble JJR. Extended Boltzmann analysis of electron swarm experiments. Phys Rev A 1981; 23: 294-304.

[73] Allis WP. Semidivergence of the Legendre expansion of the Boltzmann equation. Phys Rev A 1982, 26: 1704-12.

[74] Papadakis AP, Georghiou GE, Metaxas AC. New high quality adaptive mesh generator utilized in modelling plasma streamer propagation at atmospheric pressures. J Phys D: Appl Phys 2008; 41(23): 234019-1-12.

[75] Wikipedia, Finite Volume Method. [Retrieved 2011 February] http://en.wikipedia.org/wiki/Finite_volume_method

[76] Wolfram Mathworld, Finite Volume Method [Retrieved 2011 February]. Available at: http://mathworld.wolfram.com/FiniteVolumeMethod.html

[77] Consistency - stability - convergence [Retrieved 2011 March]. Available at: http://www.astro.uu.se/~bf/course/numhd_course/2_3_15Consistency_stability.html.

[78] Finite volume method for solving differential equations [Retrieved 2011 February] Available at: http://www.cs.cmu.edu/~scandal/nesl/demos/hw6/node3.html

[79] Papadakis AP, Georghiou GE, Metaxas AC. Simulation for the transition from non-thermal to thermal discharges. Plasma Sources Sci Technol 2005; 14: 250-8.

[80] Morrow R, Lowke JJ. Streamer propagation in air. J Phys D: Appl Phys 1997; 30: 614-27.

[81] Kunhardt EE, Tzeng Y. Development of an electron avalanche and its transition into streamers. Phys Rev A 1988; 38: 1410-21.

[82] Steinle G, Neundorf D, Hiller W, Pietralla M. Two-dimensional simulation of filaments in barrier Discharges. J Phys D: Appl Phys 1999; 32: 1350-6.

[83] Naidis GV. On photoionization produced discharges in air. Plasma Sources Sci Technol 2006; 15: 253-5.

[84] Zheleznyak MB, Mnatsakarian AK, Sizykh SV. Photoionisation of nitrogen and oxygen mixtures by radiation from gas discharges. High Temp 1982; 20: L1-6.

[85] Teich TB. Emission of gas ionizing radiation from electron avalanches. Z Phys 1967; 199: 378-410.

[86] Kulikovsky AA. The role of the absorption length of photoionizing radiation in streamer dynamics in weak fields: a characteristic scale of ionization domain. J Phys D: Appl Phys 2000*;* 33: L5-7.

[87] Aints M, Haljaste A, Roots L. Photoionizing radiation of positive corona in moist air. Proceedings VIII International Symposium High Pressure Low Temperature Plasma Chemistry; 2002, Tartu: Estonia: Tartu University Press, pp. 282-5.

[88] Hallac A, Georghiou GE, Metaxas AC. Three-dimensional characterization of short-gap streamers in air at atmospheric pressure. IEEE Trans Plasma Sci 2005; 33(2): 268-9.

[89] Hallac A, Georghiou GE, Metaxas AC. Secondary emission effects on streamer branching in transient non-uniform short-gap discharges. J Phys D: Appl Phys 2003; 36: 2498-509.

[90] Penney WG, Hummert GT. Photoionisation measurement in air, oxygen and nitrogen. J Appl Phys 1970; 41(2): 572-6.

[91] Georghiou GE. Gas discharge modeling. Using the finite-element flux corrected transport method. PhD thesis. Emmanuel College. Department of Electrical Engineering, University of Cambridge, March 2000.

[92] Kang WS, Park JM, Kim Y, Hong SH. Numerical Study on Influences of Barrier Arrangements on Dielectric Barrier Discharge Characteristics. IEEE Trans Plasma Sci 2003; 31(4): 504-10.

[93] Morrow R, Sato N. The discharge current induced by the motion of charged particles in time-dependent electric fields; Sato's equation extended. J Phys D: Appl Phys 1999; 32(5): L20-2.

[94] Wikipedia, Plasma Physics [Retrieved 2011 January]. Available at: http://en.wikipedia.org/wiki/Plasma (physics).

[95] Donko Z, Rozsa K, Tobin RC. Monte Carlo analysis of the electrons' motion in a segmented hollow cathode discharge. J Phys D: Appl Phys 1996; 29(1): 105-14.

[96] Surendra M, Graves DB. Particle simulations of radio-frequency glow discharges. IEEE Trans Plasma Sci 1991; 19(2): 144-57.

[97] Takao Y, Kusaba N, Eriguchi K, Ono K. Two-dimensional particle-in-cell Monte Carlo simulation of a miniature inductively coupled plasma source. J Appl Phys 2010; 108**:** 093309-1-8.

[98] Verboncoeur JP, Langdon AB, Gladd NT. An Object-Oriented Electromagnetic PIC Code. Comput Phys Commun 1995; 87: 199-207.

[99] Verboncoeur JP, Alves MV, Vahedi V, Birdsall CK. Simultaneous Potential and Circuit Solution for 1d bounded Plasma Particle Simulation Codes. J Comput Phys 1993; 104: 321-8.

[100] Kim GJ, Iza F, Lee JK. Electron and ion kinetics in a micro hollow cathode discharge. J Phys D: Appl Phys 2006; 39: 4386-92.

[101] Iza F, Lee JK. Low-pressure plasma generation inside slender tubes. Comput Phys Commun 2007; 177: 72-5.

[102] Bogaerts A, Gijbels R, Goedheer WJ. Hybrid Monte Carlo-fluid model of a direct current glow discharge. J Appl Phys 1995; 78: 2233-41.

[103] Hong YJ, Lee SM, Kim GC, Lee JL. Modeling High-Pressure Microplasmas: Comparison of Fluid Modeling and Particle-in-Cell Monte Carlo Collision Modeling. Plasma Proces Polym 2008; 5: 583-92.

[104] Karolewski MA. Classical dynamics simulation of projectile-surface interactions. Surf Interface Anal 1999; 27: 114-22.

[105] Zhu LG, Zhang ZB, Zhu XM, Pu YK, Li ZR. Spatial non-uniformity of electron energy in a microwave atmospheric-pressure microplasma. Appl Phys Lett 2009; 94: 151502-1-3.

[106] Mariotti D, Shimizu Y, Sasaki T, Koshizaki N. Gas temperature and electron temperature measurements by emission spectroscopy for an atmospheric microplasma. J Appl Phys 2007; 101: 013307-1-8.

[107] Staack D, Farouk B, Gutsol A, Fridman F, Alexander A. Spatially resolved temperature measurements of atmospheric pressure normal microplasmas in air. IEEE Trans Plasma Sci 2007; 35(5) 1448-55.

[108] Staack D, Farouk B, Gutsol A, Fridman A. Spectroscopic studies and rotational and vibrational temperature measurements of atmospheric pressure normal low plasma surface in air. Plasma Sources Sci Technol 2006; 15(4): 818-27.

[109] Laux CO, Spence TG, Kruger CH, Zare RN. Optical diagnostics of atmospheric pressure air plasmas. Plasma Sources Sci Technol 2003; 12(2): 125-38.

[110] Laux CO. Radiative and nonequilibrium collision radiative models. Rhose Saint Genesem, Belgium von Karman Institute 2002.

[111] Papadakis AP, Georghiou GE, Metaxas AC. Two-dimensional axisymmetric simulations and the heating effects associated with DC atmospheric pressure discharges during the post-streamer stage. IEE PROC-A 2007; 1(2) 113-20.

[112] Rolf B, Olaf T, Schoenbach KH. Gas Temperature Measurements in High Pressure Glow Discharges in Air. 30th Plasma dynamics and Lasers Conference. 1999 28th June -1st July. Norfolk, VA.

[113] Zhu XM, Chen WC, Pu YK. Gas temperature, electron density and electron temperature measurement in a microwave excited microplasma. J Phys D: Appl Phys 2008; 41: 105212-1-6.

[114] Wagner HE, Kozlov KV, Brandenburg R. Cross-correlation emission spectroscopy applied to non-equilibrium plasma diagnostics. In: Hippler R, Kersten H, Schmidt M, Schoenbach KH, Eds. Low temperature plasmas – fundamentals, technologies and techniques. 2nd ed. Weinheim: WILEY-VCH, Verlag, GmbH&Co, KGaA 2008; vol. 1: pp. 271-306.

[115] Wagner HE, Brandenburg R, Kozlov KV. Progress in the Visualization of Filamentary Gas Discharges, Part 1: Milestones and Diagnostics of Dielectric-barrier Discharges by Cross-Correlation Spectroscopy. J Adv Oxid Technol 2004; 7(1): 11-9.

[116] Kozlov KV, Brandenburg R, Wagner HE, Morozov AM, Michel P. Investigation of the filamentary and diffuse mode of barrier discharges in N_2/O_2 mixtures at atmospheric pressure by cross-correlation spectroscopy. J Phys D: Appl Phys 2005; 38: 518-29.

[117] Hoder T, Sira M, Kozlov K, Wagner HE. Investigation of the coplanar barrier discharge in synthetic air at atmospheric pressure by cross-correlation spectroscopy. J Phys D: Appl Phys 2008; 41: 035212-1-9.

[118] Grosch H, Hoder T, Weltmann KD, Brandenburga R. Spatio-temporal development of microdischarges in a surface barrier discharge arrangement in air at atmospheric pressure. Eur Phys J D 2010; 60: 547-53.

[119] Wagner HE, Kozlov KV, Brandenburg R. Low temperature plasmas. Hippler R, Kersten H, Schmidt M, Schoenbach KH, Eds. Weinheim: Wiley-VCH 2008; vol. 1: pp. 271-306.

[120] Becker W. Advanced time-correlated single photon counting techniques. Berlin: Springer-Verlag 2005.

[121] Nakane M, Kuwako A, Nishizawa K, Kimura H, Konagai C, Okamura T. Analysis of trace metal elements in water using laser-induced fluorescence of laser-breakdown plasma, Proceedings SPIE-Int. Soc. Opt. Eng. 3935 (2000) 122-131, Laser plasma generation and diagnostics.

[122] Sdorra W, Niemax K. Temporal and spatial resolution of analyte atoms and ions in microplasmas produced by laser ablation of solid samples. Spectrochim Acta B 1990; 45: 917-26.

[123] Margetica V, Banb T, Leis F, Niemax K, Hergenro R. Hydrodynamic expansion of a femtosecond laser produced plasma. Spectrochim Acta B 2003; 58: 415-25.

[124] Mazouffre S, Bakker I, Vankan P, Engeln R, Schram DC. Two-photon laser induced fluorescence spectroscopy performed on free nitrogen plasma jets. Plasma Sources Sci Technol 2002; 11: 439-47.

[125] Gans T, Schaper L, Knake N, Niemi K, Schulz-von der Gathen V, Winter J. Discharge dynamics in a micro-plasma jet. 60th Gaseous Electronics Conference; 2007 October 2-5; Arlington, Virginia USA, 2007.

[126] Schaper L, Reuter S, Waskoenig J, Niemi K, Gathen VS, Gans T. The dynamics of radio-frequency driven atmospheric pressure plasma jets. 2nd Int. Workshop on Non-equilibrium Processes in Plasmas and Environmental Science, Journal of Physics: Conference Series 2009; 162: 012013-1-8.

[127] Tachibana K. Spectroscopic Characterization of Microplasmas. Final technical report. 1 Jun 2008-31 May 2009, 1-20, FA2386-08-1-4113, A915605.

[128] Oh JS, Gonzalvo YA, Bradley JW. Time-resolved mass spectroscopic studies of an atmospheric-pressure helium microplasma jet. J Phys D: Appl Phys 2011; 44: 365202-1-10.

[129] Waskoenig J, Niemi K, Knake N, Graham LM, Reuter S, Schulz-von der Gathen V, Gans T. Atomic oxygen formation in a radio-frequency driven micro-atmospheric pressure plasma jet. Plasma Sources Sci Technol 2010; 19: 045018-1-11.

[130] Benedikt J, Consoli A, Schulze M, Keudell von A. Time-Resolved Molecular Beam Mass Spectrometry of the Initial Stage of Particle Formation in an $Ar/He/C_2H_2$ Plasma. J Phys Chem A 2007; 111: 10453-1-9.

[131] Molecular Beam Mass Spectrometry, Combustion Research Facility. [Retrieved 2011 August]. Available at: https://share.sandia.gov/crf/ page.php?id=83

[132] Miura N, Hopwood J. Spatially resolved argon microplasma diagnostics by diode laser absorption. J Appl Phys 2011; 109: 013304-1-6.

[133] Miura N, Xue J, Hopwood JA. Argon Microplasma Diagnostics by Diode Laser Absorption. IEEE Trans Plasma Sci 2010; 38(9). 2458-64.

[134] Harilal SS, Tillack MS. Laser plasma density measurements using interferometry, UCSD-ENG-114, 2004 [Retrieved 2011 February] Available at: http://www-ferp.ucsd.edu/LIB/REPORT/UCSD-ENG/UCSD-ENG -114.pdf

[135] Bukin VV, Vorobev NS, Garnov SV, *et al*. Formation and development dynamics of femtosecond laser microplasma in gases. IEEE J Quantum Elect 2006; 36(7): 638-45.

[136] Tseng AA. Recent developments in micromilling using focused ion beam technology. J Micromech Microeng 2004; 14: R15-34.

[137] Wen L, Zhang Q, Xiang W, Wang H, Chu J. Design and Fabrication of the Microplasma Reactor for Maskless Scanning Plasma Etching. Proceedings of the 2009 4th IEEE International Conference on Nano/Micro Engineered and Molecular Systems; 2009 January 5-8; Shenzhen, China.

Received: August 9, 2011 Revised: September 19, 2011 Accepted: October 14, 2011